

INFORMATION TO USERS

This manuscript has been reproduced from the microfilm master. UMI films the text directly from the original or copy submitted. Thus, some thesis and dissertation copies are in typewriter face, while others may be from any type of computer printer.

The quality of this reproduction is dependent upon the quality of the copy submitted. Broken or indistinct print, colored or poor quality illustrations and photographs, print bleedthrough, substandard margins, and improper alignment can adversely affect reproduction.

In the unlikely event that the author did not send UMI a complete manuscript and there are missing pages, these will be noted. Also, if unauthorized copyright material had to be removed, a note will indicate the deletion.

Oversize materials (e.g., maps, drawings, charts) are reproduced by sectioning the original, beginning at the upper left-hand corner and continuing from left to right in equal sections with small overlaps.

Photographs included in the original manuscript have been reproduced xerographically in this copy. Higher quality 6" x 9" black and white photographic prints are available for any photographs or illustrations appearing in this copy for an additional charge. Contact UMI directly to order.

**Bell & Howell Information and Learning
300 North Zeeb Road, Ann Arbor, MI 48106-1346 USA
800-521-0600**

UMI[®]

**Mechanical Behavior of IF 409 Ferritic
Stainless Steel**

by
Ian A. DeArdo

**A Thesis Submitted to the Faculty of Graduate Studies and
Research in Partial Fulfillment of the Requirements for the
Degree of Master of Engineering**

**Department of Mining and Metallurgical Engineering
McGill University
Montreal, Quebec, Canada**

August 1998

© Copyright



National Library
of Canada

Acquisitions and
Bibliographic Services

395 Wellington Street
Ottawa ON K1A 0N4
Canada

Bibliothèque nationale
du Canada

Acquisitions et
services bibliographiques

395, rue Wellington
Ottawa ON K1A 0N4
Canada

Your file Votre référence

Our file Notre référence

The author has granted a non-exclusive licence allowing the National Library of Canada to reproduce, loan, distribute or sell copies of this thesis in microform, paper or electronic formats.

The author retains ownership of the copyright in this thesis. Neither the thesis nor substantial extracts from it may be printed or otherwise reproduced without the author's permission.

L'auteur a accordé une licence non exclusive permettant à la Bibliothèque nationale du Canada de reproduire, prêter, distribuer ou vendre des copies de cette thèse sous la forme de microfiche/film, de reproduction sur papier ou sur format électronique.

L'auteur conserve la propriété du droit d'auteur qui protège cette thèse. Ni la thèse ni des extraits substantiels de celle-ci ne doivent être imprimés ou autrement reproduits sans son autorisation.

0-612-50600-2

Canada

Abstract

IF 409 stainless steel is a common industrial steel grade used in automotive exhaust systems. It combines a high formability with the corrosion resistance associated with stainless steels. Two particular grades of IF 409 were used in these experiments: a titanium stabilized and a titanium-niobium stabilized. The current work explores the mechanical behavior of this grade with emphasis on the occurrence of dynamic recrystallization. Hot torsion tests were performed over a range of temperatures and strains to determine the behavior. The tests were analyzed using the flow curves, optical microscopy, and texture measurements. The optical micrographs indicated that dynamic recrystallization was occurring. The texture results confirmed that the titanium stabilized steel dynamically recrystallized around 1000°C and the titanium-niobium grade recrystallized around 1200°C. In addition, the effects of strain and temperature were quantified. The results allow the feasibility of dynamic recrystallization in industrial applications to be determined.

Résumé

Les aciers inoxydables 409 IF sont des aciers ferritiques communs utilisés dans l'industrie automobile pour les conduites d'échappement des fumées. Ils associent une bonne formabilité avec une bonne résistance à la corrosion, comparable aux aciers inox de la série austénitique 304. Deux nuances de 409 IF ont été étudiées: une stabilisée au titane, l'autre au titane-niobium. Le présent travail explore les propriétés mécaniques de ces nuances avec une attention particulière pour la recristallisation dynamique. La microscopie optique a mis en évidence la présence de ce type de recristallisation. Les textures résultantes confirment qu'autour de 1000°C la nuance titane recristallise dynamiquement alors que la nuance titane-niobium ne recristallise qu'à partir de 1200°C. De plus, les effets de la quantité de déformation et de la température ont été étudiés. Les résultats montrent que la recristallisation dynamique pourrait être utilisée lors de procédés de déformation industriels qui restent à déterminer.

Acknowledgments

I would like to thank the many people who were so helpful and kind to me during my time at McGill. First, I wish to express my deep gratitude to my supervisors, Professors J.J. Jonas and S. Yue. They provided an excellent environment in which to work, generously supplying help, experience, and kindness throughout my research. I would especially like to thank them for their patience during the writing of my thesis which went well beyond anything I could have expected.

I would also like to thank the MMPC group for providing me with the Centre scholarship. The people who make up the group have my utmost thanks and respect. I would especially like to thank Dr. T. Maccagno for all of his help with my mechanical testing. Edwin Fernandez deserves a very special mention for his extra efforts as group technician. I would also like to thank Lorraine Mello for providing limitless administrative help and a wonderfully cheery disposition. Dr. Jerzy Baczynski played a very large role in my work. Not only did he produce the work upon which mine was built, but he was a constant source of help and suggestions, as well as being a great friend. Finally, I would like to thank my fellow students who provided a great

atmosphere for me at McGill and Montreal in general. I wish I could name them all as they all deserve it, but I would like to pick out Andy, Priti, Alain, Norm, Leo, Matt, and Abbas. I would also like to especially thank the parents of Andy for providing me with a home away from home.

Finally, I would like to thank my family. I can't begin to thank my parents for providing me the ability, opportunities, and, especially, the vision to do this work. I would also like to thank my extended family for all of their support!

To everyone I left out, please accept my apologies and thanks.

Table of Contents

Abstract	i
Résumé	ii
Acknowledgments	iii
Table of contents	v
List of figure captions	viii
List of table headings	xi
Chapter 1: Introduction	1
Chapter 2: Literature Review	4
2.0 Introduction	4
2.1 Classification	4
2.1.1 Ferritic Stainless Steel	5
2.1.2 Austenitic Stainless Steel	6
2.1.3 Martensitic Stainless Steel	6
2.1.4 Manganese Substituted Austenitic Stainless Steel	6
2.1.5 Duplex Austenitic-Ferritic Stainless Steel	6
2.1.6 Precipitation-hardening Stainless Steel	7
2.2 Development of Stainless Steel Chemistries	7
2.3 General Characteristics of Ferritic Stainless Steels	8
2.4 Interstitial Free Steel Characteristics	11
2.5 Fundamentals of Mechanical Behavior and Properties	11
2.5.1 Stored Energy of Deformation	12
2.5.2 Softening Mechanisms	13

2.5.2.1	Dynamic Recovery.....	14
2.5.2.2	Dynamic Recrystallization.....	14
2.5.2.2.1	Nucleation of Dynamic Recrystallization.....	16
2.5.2.2.2	Dynamic Recrystallization in Ferritic Stainless Steels.....	17
2.5.3	Static Recovery.....	19
2.5.4	Static Recrystallization.....	20
2.5.4.1	Nucleation.....	21
2.5.4.2	Growth.....	23
2.5.4.2.1	Kinetics of Static Recrystallization...	24
2.5.6	Post-Dynamic Static Recrystallization.....	25
2.5.7	Effect of Stacking Fault Energy on Softening.....	25
2.6	Formability.....	26
2.7	Texture.....	27
2.7.1	Texture Representations.....	28
Chapter 3:	Experimental Procedure.....	29
3.0	Background.....	29
3.1	Materials.....	29
3.2	Torsion Testing.....	30
3.2.1	Softening Behavior Characterization.....	32
3.2.2	Continuous Torsion Tests.....	34
3.3	Texture Sample Preparation.....	36
3.4	Metallographic Analysis.....	37
3.5	Texture Measurement.....	37
Chapter 4:	Experimental Results.....	39
4.1	Softening Kinetics.....	39

4.2	Flow Curves.....	41
4.3	Microstructural Observations.....	43
4.4	Texture Measurements.....	45
Chapter 5:	Discussion.....	74
5.1	General.....	74
5.2	Room Temperature.....	75
5.3	Elevated Temperature Mechanical Behavior.....	75
5.4	Microstructural Analysis at Elevated Temperatures.....	76
5.5	Torsion Textures at Elevated Temperatures.....	77
5.6	Importance of the D2 Component.....	81
5.7	Continuous Dynamic Recrystallization.....	83
5.8	Static Recrystallization Kinetics.....	84
5.9	Effect of Chemical Composition.....	84
Chapter 6:	Conclusions.....	86
References.....		89

List of Figures

Fig. 2.1	Effect of composition on gamma loop.....	8
Fig. 2.2	Fe-Cr phase diagram.....	10
Fig. 2.3	Photo of automotive exhaust (manifold) system.....	11
Fig. 2.4	Schematic illustrating dynamic recovery at elevated temperatures.....	14
Fig. 2.5	Stress-strain curve illustrating salient points of dynamic recrystallization.....	15
Fig. 2.6	Necklacing during dynamic recrystallization.....	17
Fig. 2.7	Effect of grain boundary angle on mobility.....	22
Fig. 2.8	Subgrain coalescence model of Hu.....	22
Fig. 2.9	Strain induced boundary migration.....	23
Fig. 3.1	Schematic of torsion test sample.....	30
Fig. 3.2	Schematic of torsion test equipment.....	31
Fig. 3.3	Schematic representation of the 0.2% offset method for calculating the softening kinetics.....	33
Fig. 3.4	Test schedule for torsion samples.....	35
Fig. 3.5	Sample reference system in torsion.....	37
Fig. 3.6	The pole figures are oriented with respect to the θ , z , and r axes of the sample.....	37

Fig. 4.1	Softening curve of Ti IF 409.....	40
Fig. 4.2	Softening curve of Ti-Nb IF 409.....	40
Fig. 4.3	Both steels deformed at room temperature.....	41
Fig. 4.4	Flow curves of Ti IF 409 at various temperatures.....	42
Fig. 4.5	TiNb IF 409 deformed at various temperatures.....	43
Fig. 4.6	Microstructures of Ti IF 409.....	44
Fig. 4.7	Microstructures of TiNb IF 409.....	46
Fig. 4.8	{110} pole figure displaying the ideal orientations observed during the present torsion tests.....	48
Fig. 4.9	Ti IF 409 deformed at RT.....	51
Fig. 4.10	TiNb IF 409 deformed at RT.....	52
Fig. 4.11	Ti IF 409 deformed at 400 C.....	54
Fig. 4.12	Ti IF 409 deformed at 500 C.....	55
Fig. 4.13	Ti IF 409 deformed at 600 C.....	56
Fig. 4.14	Ti IF 409 deformed at 700 C.....	57
Fig. 4.15	Ti IF 409 deformed at 800 C to low strain level.....	59
Fig. 4.16	Ti IF 409 deformed at 800 C to high strain level.....	60
Fig. 4.17	Ti IF 409 deformed at 900 C to low strain level.....	61
Fig. 4.18	Ti IF 409 deformed at 900 C to high strain level.....	62
Fig. 4.19	Ti IF 409 deformed at 1000 C to low strain level.....	63
Fig. 4.20	Ti IF 409 deformed at 1000 C to high strain level.....	64
Fig. 4.21	Ti IF 409 deformed at 1100 C to low strain level.....	65

Fig. 4.22	Ti IF 409 deformed at 1100 C to high strain level.....	66
Fig. 4.23	TiNb IF 409 deformed at 700 C.....	68
Fig. 4.24	TiNb IF 409 deformed at 800 C.....	69
Fig. 4.25	TiNb IF 409 deformed at 900 C.....	70
Fig. 4.26	TiNb IF 409 deformed at 1000 C.....	71
Fig. 4.27	TiNb IF 409 deformed at 1100 C.....	72
Fig. 4.28	TiNb IF 409 deformed at 1200 C.....	73
Fig. 5.1	Ti stabilized IF 409: effect of temperature on critical component intensity.....	79
Fig. 5.2	TiNb stabilized IF 409: effect of temperature on critical component intensity.....	80
Fig. 5.3	Effect of temperature on D2 components of various IF steel grades.....	82

LIST OF TABLE CAPTIONS

Table 2.1	Typical compositions of selected stainless steel classifications.....	5
Table 3.1	Chemical compositions of the experimental materials.....	30
Table 4.1	Test matrix.....	47
Table 4.2	Some important torsion ideal orientations.....	47
Table 4.3	Experimental ODF intensities for some important orientations in the Ti stabilized IF 409.....	49
Table 4.4	Experimental ODF intensities for some important orientations in the TiNb stabilized IF 409.....	50

Chapter I

INTRODUCTION

Stainless steels can be divided into two major types: austenitic (300 grade) and ferritic (400 grade). Currently, austenitic stainless steel grades are the more extensively used in industry. This situation arises because the mechanical properties are superior over a range of temperatures. However, the use of the austenitic grades is limited worldwide because of the high cost due to the relatively large amount nickel present. Ferritic stainless steels are widely used as sheet in the automotive industry (approximately 250,000 tons/year of 409). The principal uses for ferritic stainless steel sheet in the automotive industry are in exhaust systems, exterior trim, and mufflers. Ferritic stainless steel is ideal for these applications because of its adequate corrosion resistance, excellent high temperature resistance to oxidation, good weldability and forming characteristics. In addition to its automotive uses, 409 is used in smaller amounts in the food and hospital industries, furnishings, transportation, and chemical industry applications.

Ferritic stainless steels have certain advantages over competing materials (such as austenitic stainless steels, superalloys, and standard carbon steels), namely lower alloy content (hence the lower cost), excellent resistance to pitting and crevice corrosion caused by chlorides, and they

Chapter I Introduction

have remarkable corrosion resistance in other environments (organic acids, urea production, and caustic environments).

When compared to the mechanical properties of austenitic stainless steels, the ferritic steels typically have a higher yield strength, but a lower work-hardening rate. This characteristic makes ferritic stainless steel much less suitable than austenitic stainless steels for applications involving forming by stretching. However, ferritic stainless steels are more easily formed at room temperature by most methods.

Ferritic stainless steels have a much higher stacking fault energy, which tends to encourage recovery over recrystallization. This tendency makes the improvement of properties by grain refinement extremely difficult. However, recent work has suggested that a 'window', or certain range of thermomechanical processing variables, of recrystallization does indeed exist in interstitial free 409 stainless steel and in conventional interstitial free steels. Thus, thermomechanical processing in this 'window' could be used to control and improve the final properties of the steel.

The primary objective of this work, then, is to determine the thermomechanical processing (TMP) variables where dynamic recrystallization will occur. In addition, the effect of stabilizing elements, such as niobium and titanium, on the recrystallization behavior of the ferritic stainless steel was examined. The experiments were performed on two steels, one titanium stabilized and one titanium and niobium stabilized. These steels were deformed in a hot torsion machine to attempt to generate dynamic recrystallization. The latter was characterized from the flow curves, microstructure, and texture analysis.

Chapter I Introduction

In chapter 2, the current understanding of the important concepts involved in this work is discussed. Chapter 3 provides the relevant information about the experiment procedure and methods used in this work. The results of these experiments are listed in chapter 4. Chapter 5 contains the discussion of these results. Finally, the conclusions are provided in chapter 6.

Chapter II

Literature Review

2.0 Background

Unlike typical steel grades, stainless steels are not designed for mechanical properties or formability, but rather for their corrosion and oxidation resistance. The 'stainless' appellation arises from the resistance to staining, rusting, and pitting in air. This property requires the addition of from 11 to 30% chromium, with other alloying elements improving the stainless characteristics.

2.1 Classification

The classifications are based upon chemical composition and other properties. Typically, six different types are identified in the literature; ferritic, austenitic, martensitic, manganese-substituted austenitic, duplex austenitic-ferritic, and precipitation-hardening stainless steels [1]. The typical ranges of compositions are listed in Table 2.1.

Table 2.1 Typical compositions of selected stainless steel classifications.

Name	Cr (wt%)	Ni	C	Mn	Si
316 Austenitic	16-18	10-14	0.08	2.0	1.0
409 Ferritic	10.5-11.75	-	0.08	1.0	1.0
403 Martensitic	11.5-13	-	0.15	1.0	0.5
329 Duplex	26	5.0	0.08	-	-
630 Precipitation- Hardening	16	4.0	0.4	0.25	0.60

2.1.1 Ferritic

The name for this classification arises from the crystallographic structure of this family. Typically, ferritic stainless steels contain between 11 and 29% chromium and very low carbon levels. This family is characterized in the lower chromium range by fair corrosion resistance and good formability at a low cost. The higher chromium content ferritic stainless steels are used in applications requiring a high resistance to oxidation and corrosion. However, poor weldability limits their use, even with very low carbon levels.

Chapter II Review

2.1.2 Austenitic

As with the ferritic grades, the austenitic name originates from the crystallographic structure. High levels of nickel are added to this steel grade for corrosion resistance, which stabilizes the austenitic structure at all temperatures and leads to a high cost. This grade has an inherently strong corrosion resistance and good formability because of the FCC structure. Another advantage of this grade is the relative ease of recrystallization, which allows for better control of the mechanical properties.

2.1.3 Martensitic

These grades use the quench and temper process to achieve very high strengths with reasonable ductility. Because of the high alloy content, these steels have a superior hardenability. The advantage of the high hardenability often leads to degradation of the corrosion resistance.

2.1.4 Manganese Substituted Austenitic Stainless Steel

Similar to the standard austenitic stainless steels, this steel relies on the austenite stabilizing property of manganese in lieu of a completely nickel-based stabilization. The main difference in properties from austenitic stainless steels is higher strength.

2.1.5 Duplex Austenitic-Ferritic Stainless Steel

Unlike the other stainless steels (typically), this steel is a marriage of both the austenitic and ferritic phases. The mechanical and corrosion

properties are a blend of those of the component phases. The result is desirable corrosion and mechanical properties.

2.1.6 Precipitation-hardening Stainless Steels

These steels use a composition that encourages precipitation in either a martensite or austenite matrix. The precipitation increases the strength of the steel so that these steels have the highest strengths and operating temperatures.

2.2 Development of Stainless Steel Chemistries

While the iron-carbon system has major advantages in the combination of strength, ductility, toughness, formability, and low cost, one of the principal problems of the system is the susceptibility to corrosion and oxidation. Possibly the first observation of the effect of chromium additions to iron was made by Berthier in 1821 [2]. He also noticed that increased amounts of chromium led to even better corrosion resistance. One of the driving applications at this time was in the cutlery industry. Berthier's 1.5% Cr steel had high hardness with superior corrosion resistance to carbon steels. However, researchers were unable to determine "optimum" compositions due to experimental inconsistency because of the vague definition of "stainless" steels. At the beginning of this century, several researchers from France and Germany published works on chromium steels [3-5]. Between 1900 and 1909, these researchers concentrated on ferritic (13% Cr) and martensitic (17%) stainless steels. In 1909, the French metallurgist Guillet published work on the chromium-nickel austenitic stainless steels. Subsequent work, notably that of Monnartz from Germany [6], outlined the actual role of chromium and carbon on passivity. The practical trials of these steels were first

performed from 1910 to 1915. The understanding of stainless steels progressed slowly but steadily over the ensuing years. During the Second World War, the substitution of nickel by manganese and nitrogen were investigated due to shortages in Europe. Precipitation-hardening stainless steels, while investigated in the 1930s, have been heavily researched and developed only recently.

2.3 General Characteristics of Ferritic Stainless Steels

Ferritic stainless steels have a chromium content ranging from 11 to 29%, but are more likely found with chromium contents in the 17 to 26% range. The balance is mainly iron. A simple iron-chromium alloy would be fully ferritic up to the melting point with chromium contents greater than or equal to 17% [7]. However, the addition of 0.1% carbon will cause austenite particles or 'stringers' above 1000°C. The amount of austenite depends on the carbon and nitrogen levels in the system and the presence of austenite stabilizing and ferrite stabilizing elements present. As would be expected, the amount of austenite increases to a maximum and then decreases again with increasing temperature, Fig 2.1 [8].

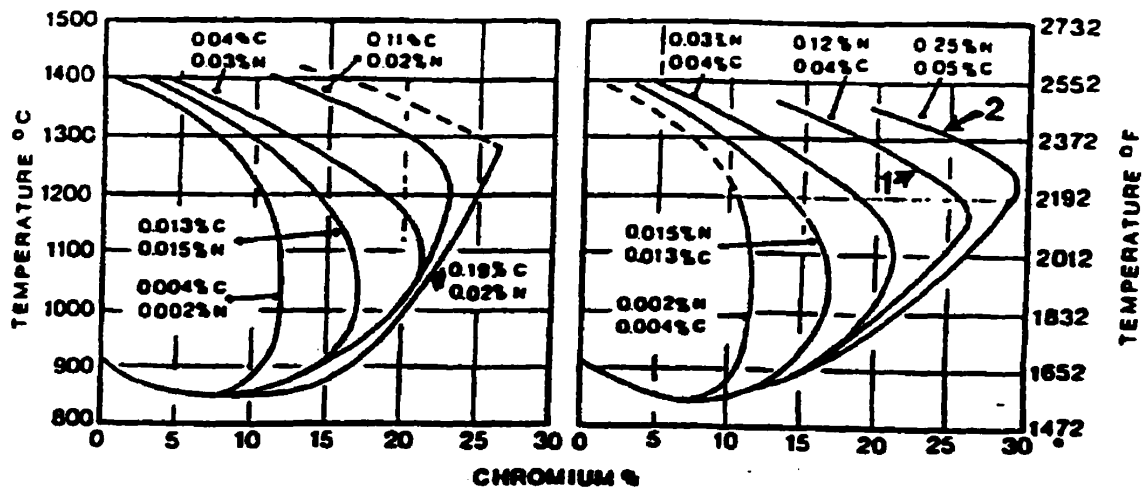


Figure 2.1 Effect of Composition on gamma loop [8].

Chapter II Review

One of the problems of ferritic stainless steels is that above 1140°C, the 17% Cr steels become fully ferritic and grain coarsening increases. During cooling, austenite typically precipitates at the ferrite grain boundaries as a Widmanstatten structure. This adversely affects the weldability of the steel, as these austenite particles transform to martensite upon cooling to room temperature.

Another problem characteristic of all stainless steels is sensitization, although it is typically associated with austenitic stainless steels. In ferritic stainless steels, sensitization results from quenching from temperatures above 925°C. This condition often arises from welding. When sensitization occurs, carbon in solution combines with the chromium also in solution to form precipitates. Since mobility for alloying elements is highest near the grain boundaries, the regions nearest the grain boundaries may lose enough chromium in solution to be susceptible to intergranular corrosion. This intergranular corrosion can lead to premature failure of the material. The addition of alloying elements such as niobium and/or titanium can prevent this behavior. The carbon and nitrogen in solution react preferentially with these elements. The latter precipitate out of solution as carbides or carbonitrides, preventing reaction with the chromium needed in solution [1,9].

An added problem in ferritic stainless steels is what is known as 475°C embrittlement. If ferritic stainless steels are exposed to or cooled through the 400-565°C temperature range, a noticeable decrease in ductility occurs. As the chromium level increases, the ductility drop increases. This decrease in ductility is generally believed to be a result of the formation of a coherent, very fine, chromium-rich body centered cubic phase. This phase is formed in the miscibility gap in the iron-carbon system by spinodal decomposition, Fig 2.2 [10]. When this occurs, the

steel is generally unusable and has to undergo a heat treatment above 590°C with a subsequent rapid cool [1,11].

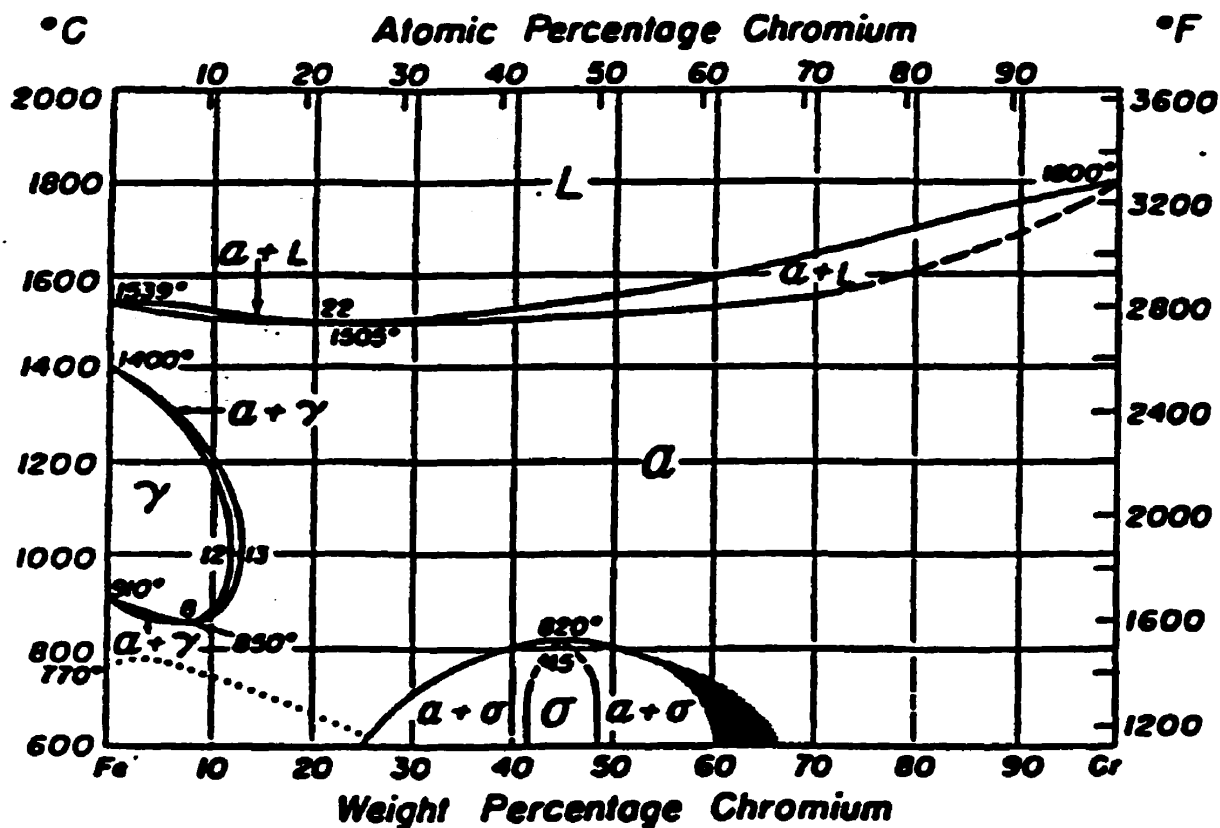


Figure 2.2 Fe-Cr phase diagram [10].

Finally, sigma-phase embrittlement presents difficulties in the application and production of higher carbon ferritic stainless steels. Like 475°C embrittlement, sigma-phase embrittlement is the occurrence of another hard, brittle phase in a certain temperature range. In this case, at temperatures between 540 and 870°C, sigma phase slowly forms preferentially along grain boundaries. Also like the other form of embrittlement, the steel is unusable in this state and the situation can be rectified by heat treatments, in this case above 900°C [1].

2.4 Interstitial Free Steel Characteristics

Interstitial free 409 stainless is characterized by the low levels of carbon and nitrogen. These low levels are critical in this grade because of the formability requirements. In Figure 2.3, the complex shapes necessary are illustrated. In order to increase the formability even further, alloying additions are included in the chemistry in order to remove the carbon and nitrogen from solution. The combination of these elements leads to the formation of precipitates, leaving an iron-chromium matrix. This is known as stabilization and is also critical, as mentioned above, in resistance to sensitization.



Figure 2.3 Photo of automotive exhaust (manifold) system.

2.5 Fundamentals of Mechanical Behavior and Properties

The driving force for softening is the stored energy due to deformation. The most common softening mechanisms are recovery and recrystallization. Recovery is a result of dislocation interactions and rearrangements. Recrystallization involves the formation of strain-free

grains and the subsequent destruction of surrounding deformed grains. These metallurgical phenomena will be described in the following sections.

2.5.1 Stored Energy of Deformation

The stored energy of deformation is the energy remaining in the system after an applied strain. Most of the energy of deformation is used in the shape change or the production of heat. However, about 1 to 5% of the energy used in deformation remains. Obviously, this higher energy state is unstable and the softening mechanisms occur to lower it [17-19].

The cause of the increase in energy of the system is due to the creation of various types of defects. These defects include dislocations, point defects, stacking faults, twins, ordered regions, and precipitates, in addition to the elastic strains present. The dislocations formed by deformation begin to move on their slip systems and interact with other dislocations, grain boundaries, solutes, or particles in the matrix forming dislocation tangles or 'pile-ups'. In some cases, especially in BCC systems, cross-slip can occur to allow the movement of the dislocations on the cross-slip plane. The strength of the material will increase during deformation if dislocation movement becomes more difficult. This is known as work hardening.

The amount of energy retained by cold work depends on several factors [13], the purity of the metal being one of them. The presence of alloy or impurity atoms in the metal allows a larger amount of energy to be stored. The process by which deformation is performed has a large effect on the stored energy. The more complex the deformation, meaning the complexity of stress gradients, strain rates, and frictional effects along with others, the larger the stored energy in the system. The temperature of

deformation also strongly affects the amount of stored energy. Work hardening rates increase at lower temperatures because of the lack of thermal activation energy available to assist dislocation movement. At high temperatures, the stored energy is actually released, depending on the activation energy of the defects present. Finally, the grain size of the metal plays a role in the amount of stored energy of cold work. Suffice it to say that the deformation of a small grain is more complicated than that of a large grain because of the greater interaction with surrounding grains.

2.5.2 Softening Mechanisms

As mentioned above, softening, either by recovery or recrystallization, occurs to reduce the energy added by deformation. As a further complication, this softening can occur either during deformation (dynamic) or after deformation (static or post-dynamic). The focus of this review will be on the softening behavior in BCC metals [12,13,18,20].

2.5.2.1 Dynamic Recovery

Dynamic recovery is the process of reorganization of dislocations into a lower energy configuration. This process occurs by several different mechanisms depending on temperature and material. Dislocations of opposite signs either annihilate each other by combination or rearrange into a subgrain or cell structure consisting of a low dislocation density core surrounded by a higher dislocation density boundary region. This phenomenon is facilitated by cross-slip and dislocation climb at higher temperatures, Fig 2.4 [12]. It is important to note that dynamic recovery occurs in the early stages of deformation and continues throughout the deformation.

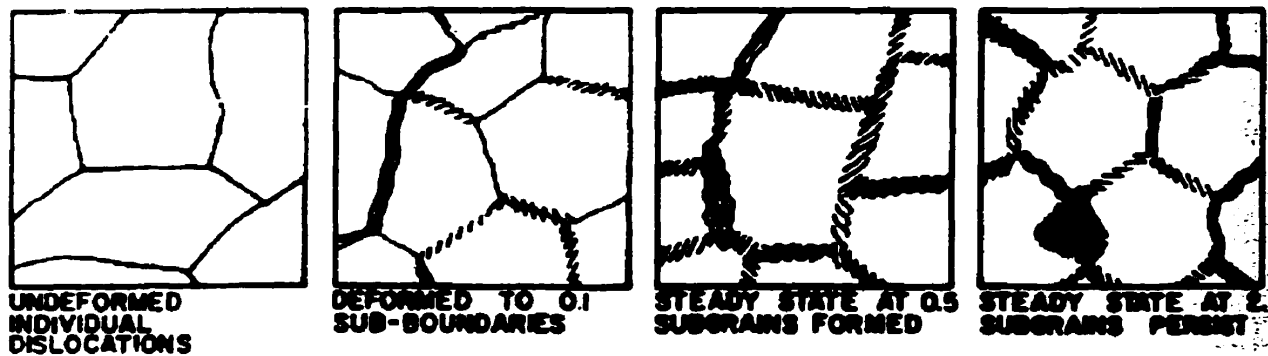


Figure 2.4 Schematic illustrating dynamic recovery at elevated temperatures [12].

In high stacking fault energy materials like ferritic stainless steel, dynamic recovery occurs rapidly due to the ease of cross-slip. This leads to a steady state, balancing work hardening with softening occurring due to rapid rearrangement of these dislocations. The steady state subgrain size depends upon the strain rate and temperature [21]. However, in lower stacking fault energy materials, recovery occurs at a much slower pace and to a lesser degree, allowing work hardening and stored energy to increase to higher levels [12].

2.5.2.2 Dynamic Recrystallization

Dynamic recrystallization relies on the stored energy remaining after dynamic recovery reaches a maximum attainable level (which is lower than the amount of energy input by deformation, obviously). In most steel systems in the austenitic region, the energy input is higher than that dissipated by dynamic recovery. When this level reaches a critical point, new strain-free grains are nucleated during the deformation. This phenomenon is known as dynamic recrystallization. However, in most high

stacking fault materials, the softening achieved by dynamic recovery is so high as to prevent the critical energy level from being reached. The most common method of determining the occurrence of dynamic recrystallization is by examining the flow curve. Typical dynamic recrystallization is characterized by the presence of a peak (or peaks) in the stress-strain curve, followed by a steady state, Fig 2.5 [22]. In certain cases, multiple peaks are reached.

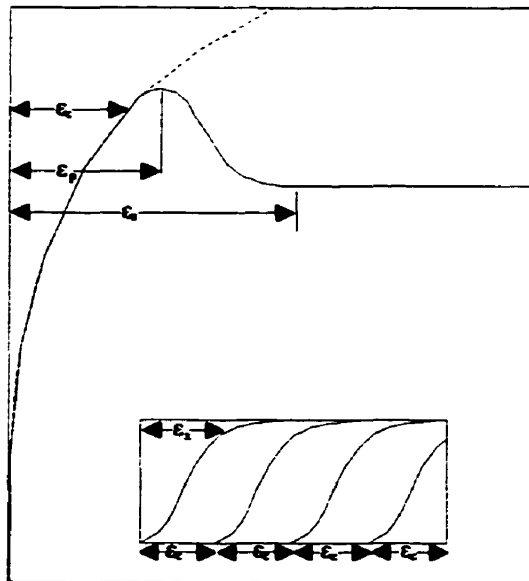


Figure 2.5 Stress-strain curve illustrating salient points of dynamic recrystallization [22].

2.5.2.2.1 Nucleation of Dynamic Recrystallization

Nucleation is typically said to begin at a critical strain, ϵ_c ($\epsilon_c=0.8\epsilon_p$) [23,24]. This value represents the amount of stored energy required to overcome the barrier to nucleation [25,26]. The dislocation density required for nucleation depends upon strain rate, temperature, chemical composition, and other factors. At low strain rates, dynamic recrystallization is nucleated by the bulging of pre-existing grain boundaries [27,28]. Nucleation at higher strain rates occurs by growth of the high angle boundary cells formed by dislocation interaction as described above [29,30]. The driving force for the migration of the boundaries is the difference in dislocation density (and, thus, stored energy) between the highly deformed matrix ahead and the less highly-deformed matrix behind this boundary [25,26]. In general, the preferential sites for nucleation occur along the existing grain boundaries. This behavior is described as 'necklacing', referring to the band of fine, new grains surrounding an older, deformed grain. These new grains grow into the older grain until impingement with other growing grains takes place. Once all of the grain boundary sites are occupied, new grains are formed at the boundary between the recrystallized and unrecrystallized grains, Fig 2.6 [31].

Dynamic recovery is an important precursor to dynamic recrystallization. The substructures formed during recovery are the basis for the nucleation sites in recrystallization [32-34].

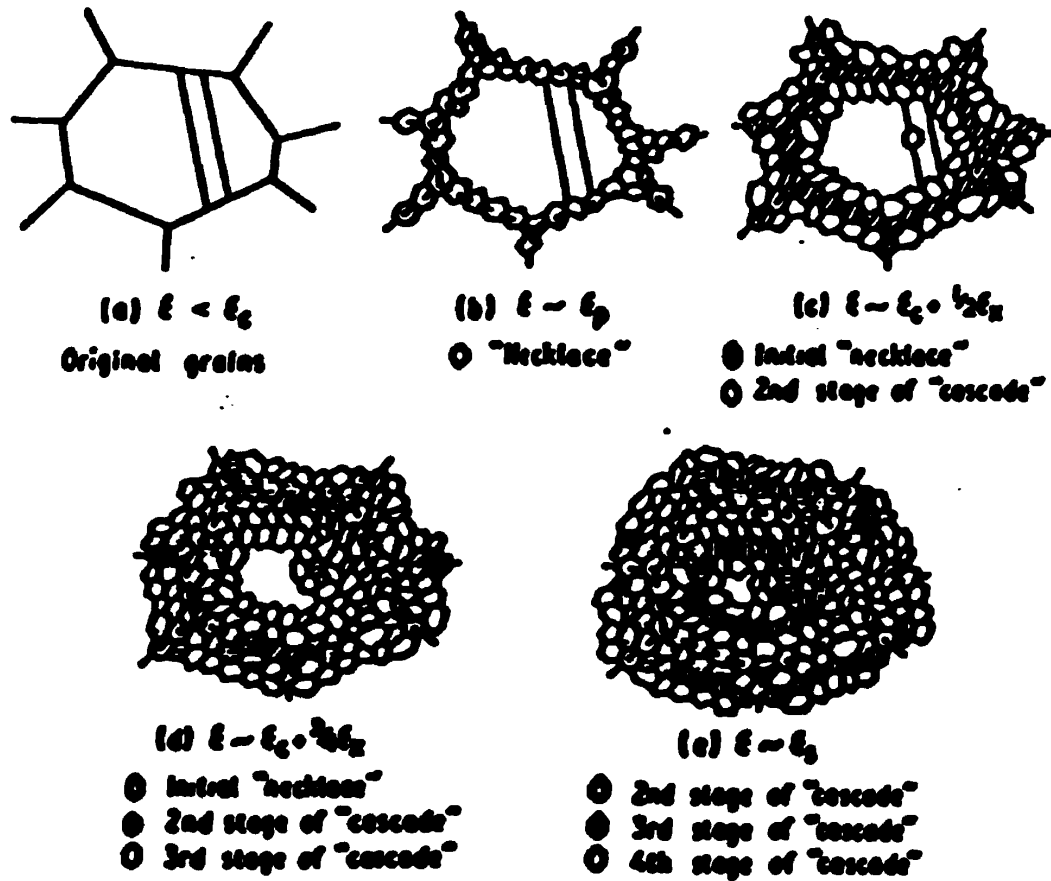


Figure 2.6 Necklacing during dynamic recrystallization [31].

2.5.2.2.2 Dynamic Recrystallization in Ferritic Stainless Steels

One important point relevant to the system under investigation is the effect a high stacking fault energy has on the dynamic recrystallization behavior. As mentioned above, high stacking fault energy metals tend to recover to a high degree. This propensity limits the possibility of dynamic recrystallization by removing most of the driving force so a critical level is never reached. In fact, dynamic recrystallization has only rarely been noted for most BCC metals [35,36]. However, in the work on similar

material by McQueen *et al.* [37,38], results showing the localized occurrence of dynamic recrystallization near γ -particles has been noted at temperatures above 1100°C at a strain rate of 1.0 s⁻¹. This dynamic recrystallization is evidenced by the formation of a substructure of smaller cells within the larger cells.

Further TEM investigation revealed the presence of high angle boundaries (>50°) between the proposed dynamically recrystallized grains. The γ -particles have the effect of strengthening the material and are found surrounded by a high dislocation density region. The γ -particles are surrounded by higher dislocation density regions due to incomplete recovery near the α - γ interface. The dislocation (hence, energy) concentrations can exceed the critical energy barrier for the nucleation of recrystallization. At temperatures below 1100°C, dynamic recrystallization is generally not evident, except in some very isolated areas. However, in general, the work seems to support the widely held view that widespread dynamic recrystallization is not very likely in ferritic stainless steels.

Recent work at McGill has provided some more insight into this problem. This was done by Jerzy Baczynski [39] on interstitial free carbon steels. In this excellent thesis, Baczynski reported the occurrence of dynamic recrystallization in the ferritic region. The steel employed in this work is similar to that studied in the present thesis, with the exception of the chromium in the stainless steel. These results may seem at odds with the paper mentioned above. This discrepancy does have an explanation. As the steels used in the McQueen *et al.* papers had a significantly higher carbon and nitrogen level than the steels presently used or in the Baczynski thesis, this would tend to reduce the possibility of dynamic recrystallization. In essence, results in steels with a higher interstitial content indicate the absence of dynamic recrystallization, except under

certain conditions. Steels with a lower interstitial content display dynamic recrystallization behavior. These results can be explained by the need for boundary migration during recrystallization. Any particle or solute slows or stops the progress of the boundary. Thus, a pure matrix would allow the grain boundaries to move more easily, thereby promoting recrystallization. In addition, several researchers have already noted that dynamic recrystallization can take place in α -iron [12,35,36,39].

2.5.3 Static Recovery

Static recovery is similar to dynamic recovery except that it occurs during annealing, rather than high temperature deformation. Static recovery is characterized by a decrease in the density and rearrangement of the dislocations resulting from previous cold work to lower energy configurations. The mechanism by which recovery occurs depends upon the annealing temperature.

At lower temperatures, the low activation energy mechanisms occur. These mechanisms include the migration of point defects to 'sinks' such as grain boundaries and dislocations. In addition, the point defects interact to reduce energy. Examples of this category include vacancy-interstitial combination, clustering, and pairing of like defects [13]. However, the total energy lost in these processes is a quite small portion of the total. Research has shown that only 10% of the total energy released was related to this process, specifically vacancy annihilation [40].

The annihilation and rearrangement of dislocations provide the largest energy release. At intermediate temperatures, the dislocations glide to form tangles, which are configurations of lower energy. Dislocations of opposite signs annihilate each other. The subgrains formed by the

dislocation movement in tangles begin to grow with thermal activation. The tangle boundaries form a sharper two-dimensional arrangement. These boundaries then begin to move, forming larger subgrains with a smaller total boundary area. In addition, microtwins are formed in the subgrains [18].

At higher temperatures, dislocations can begin to climb. 'Polygonization' can occur with dislocation climb and a high stacking fault energy. This happens when an excess of dislocations of one sign interacts. These dislocations arrange vertically and, eventually, these arrangements can form large subgrains. Another method by which recovery occurs at higher temperatures is by subgrain coalescence. The subgrains are often only slightly misoriented. The subgrains coalesce by rotating to a common orientation, leading to destruction of the common boundary. Finally, the subgrains can form a lower energy arrangement called 'cells'. These cells have very low dislocation densities in the center and walls consisting of dislocation tangles [41,42].

2.5.4 Static Recrystallization

As with dynamic recrystallization, static recrystallization is the process of replacing deformed grain volume with a newer, strain-free grain. This occurs by the migration of a high angle grain boundary through the deformed matrix during annealing rather than during deformation at an elevated temperature. As with dynamic recrystallization, this process occurs in two steps: nucleation and growth. Another similarity is that a necessary critical strain be reached before recrystallization can occur.

2.5.4.1 Nucleation

Nucleation occurs preferentially at high energy sites such as grain boundaries, deformation bands, and particles (precipitates and inclusions). Static recrystallization nucleation does not differ much from standard solid-solid phase changes in that the barrier to nucleation is the creation of new surface area and that the activation is thermally related [17,43]. The final result of nucleation in static recrystallization is the formation of a high misorientation angle boundary. Currently, three different nucleation mechanisms have been advanced [16,17,42]. These mechanisms are subgrain growth, subgrain coalescence, and strain-induced boundary migration.

The subgrain growth, or sub-boundary migration, model was first proposed by Cahn [44]. Small, strain-free cells are formed by dislocation climb and rearrangement. These cells grow since the difference between the energy caused by the dislocation density gradient across their boundaries is greater than the increased surface energy. The mobility of the boundary depends upon the misorientation between the cell and its neighbors. At very low ($4-5^\circ$) and moderate ($>20^\circ$) misorientations, the boundary is very mobile. However, at misorientations between 5 and 20° , the boundary is immobile, Fig.2.7 [46]. As for normal grain growth, the large subgrains grow at the expense of smaller subgrains. As the subgrains grow, the misorientation of the boundary increases to the point at which it becomes a typical high angle boundary.

The subgrain coalescence model, proposed by Hu [45], suggests that the subgrains rotate to reduce the misorientations with neighboring subgrains (Fig 2.8). When the misorientation angles are ~~similar~~, the

subgrains coalesce while the common exterior boundary increases in misorientation to become a high angle one.

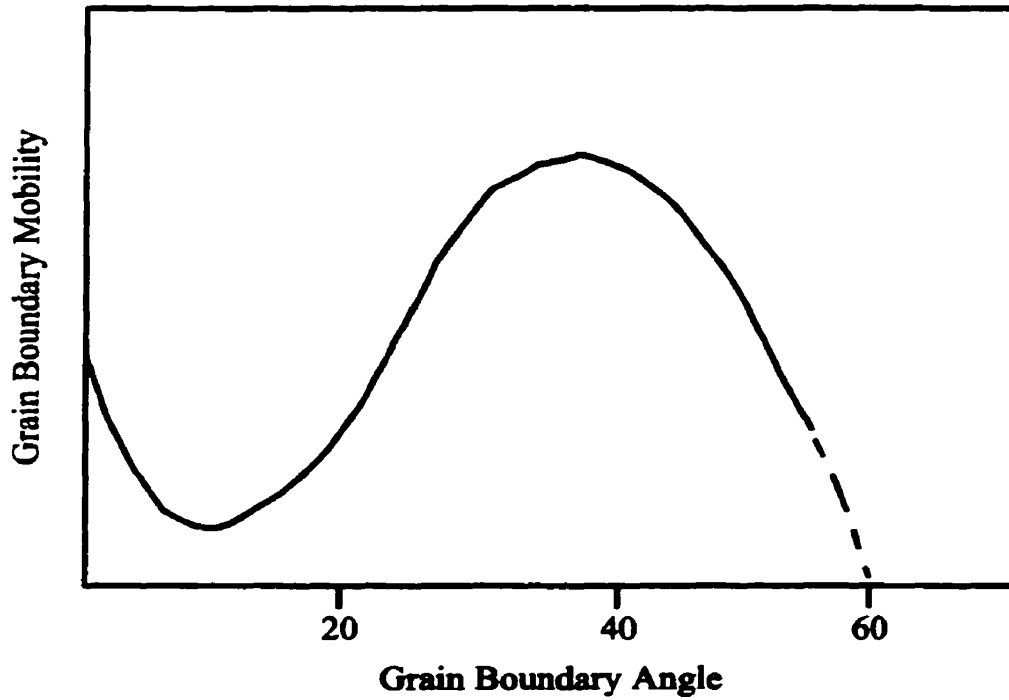


Figure 2.7 Effect of grain boundary angle on mobility [46].

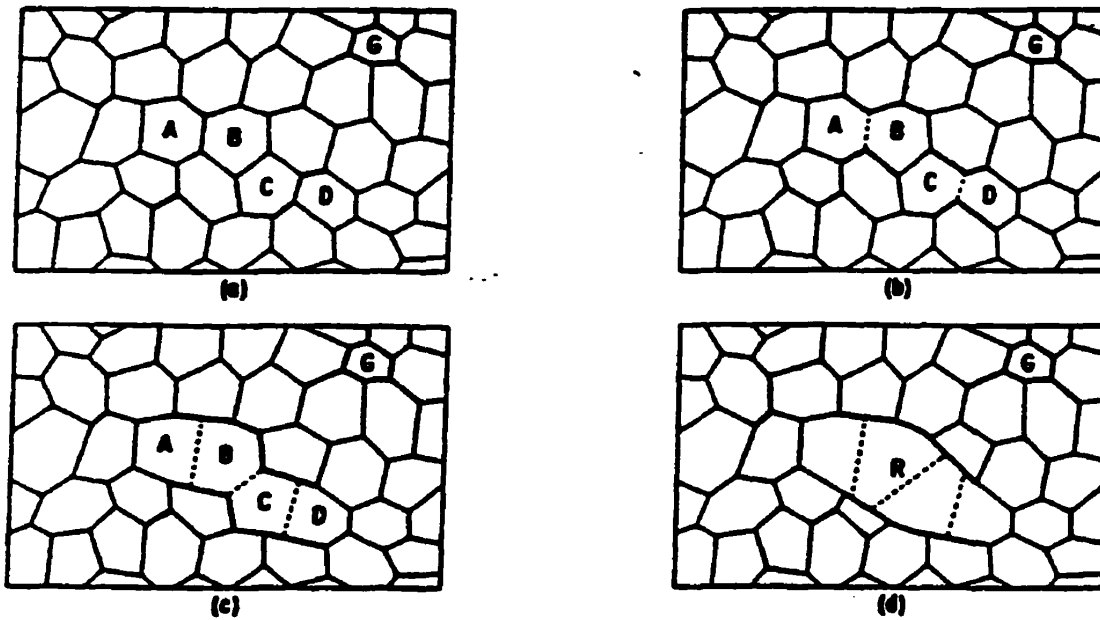


Figure 2.8 Subgrain coalescence model of Hu [45].

Beck and Sperry [47] first proposed the strain induced boundary migration model. In this model, subgrains of lower strain energy 'bulge' into ones of higher energy (Fig 2.9). Again, the driving force is the difference in strain energy across the boundary. The bulge eventually encompasses the high energy subgrain.

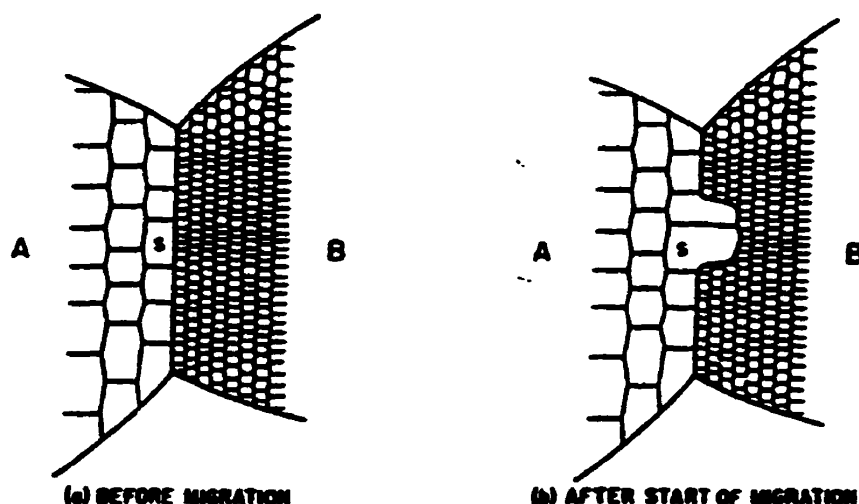


Figure 2.9 Strain induced boundary migration [47].

2.5.4.2 Growth

As with dynamic recrystallization, the nucleus expands into the surrounding deformed grains. The movement of the newly formed high misorientation angle grain boundaries depends on the matrix through which they are to move. The presence of alloying elements, both interstitial and substitutional, of particles, and the misorientation between the nucleus and the deformed grain all affect the movement of the boundary. The accepted view of the effect of alloying or impurities is that they impede the movement of the boundary by being attracted to the high energy area surrounding the boundary. The movement of the boundary and the now

associated alloy atoms is retarded when moving through the matrix of deformed grains. This can slow or stop recrystallization under these conditions. At higher temperatures or low impurity concentrations, the boundary can move quickly enough to break away from the atoms in the boundary region. In this case, recrystallization can proceed at a faster pace [16,17,43].

2.5.4.2.1 Kinetics of Static Recrystallization

Random nucleation recrystallization kinetics can be described by the Avrami equation [49]:

$$X=1-\exp(-B't^k) \quad (2.1)$$

where X is the fraction of recrystallized material at time t . B' is a constant that depends on the temperature and driving force. The exponent in the equation, k , is equal to 4 for homogeneous nucleation or 3 in the case of site saturation in 3 dimensions. If k falls between 3 and 2, then the equation is considered to describe a 2 dimensional recrystallization process [16].

Recrystallization kinetics are commonly defined in terms of the time required for 50% recrystallization, $t_{50\%}$. This value depends on the strain, ϵ , the initial grain size, D_0 , and the temperature, T . For a plain carbon steel [50]:

$$t_{50\%}=B''\epsilon^{-4}D_0^2\exp(Q_{rxn}/RT) \quad (2.2)$$

where Q_{rxn} is the activation energy for recrystallization and R is the gas constant. From this, the fraction recrystallized can be determined using the $t_{50\%}$.

2.5.6 Post-Dynamic Static Recrystallization

The softening behavior is a derivative of static recrystallization. In this case, the nuclei are created dynamically. During the interpass interval or after the deformation, these dynamic nuclei grow statically. In addition to post-dynamic static recrystallization, the metal also undergoes typical static recovery and recrystallization. Post-dynamic static recrystallization is not believed to require incubation for nucleation so very rapid microstructural changes can occur. This tends to result in a very coarse grain size [51].

2.5.7 Effect of Stacking Fault Energy on Softening

Stacking fault energy indicates the relative ease with which dislocations can separate into partial dislocations. High stacking fault energy metals (such as ferritic stainless steels) have dislocations that easily combine as the energy required to separate widely is too high. Lower stacking fault energy metals, on the other hand, have dislocations that can separate widely. This is critical in determining the nature of the softening occurring. For recrystallization to take place, a high energy must be accumulated. This will happen if the dislocations are unable to enter lower energy configurations or, in other words, if recovery is limited. To form these lower energy configurations cross-slip is required. Cross-slip requires complete (unseparated) screw dislocations. The lower the stacking fault energy, the greater the difficulty of forming a complete dislocation. Thus, low stacking fault energy metals are more able to accumulate the energy required for recrystallization [18].

2.6 Formability

As the automotive applications in which interstitial-free ferritic stainless steel are used require demanding forming operations such as deep drawing, stretch forming, and bending, the formability of the material is quite important. Formability is a metallurgical term that has no specific, agreed definition. Some use formability to describe workability or the performance of a metal in a specific forming operation. Another definition is the ability to withstand the stresses of forming without failing. Formability can be used to describe the ease with which a material can be shaped.

The aim of improved formability provides the driving force for the current work. For those interested in a specific relationship between formability and material properties, several excellent references are available [52-56]. Lankford et al. determined that the ratio of the width strain to the thickness strain of a tension test specimen was an important parameter in predicting the press performance of deep drawing carbon steel sheets during the pressing of certain automotive components. This ratio, R , which is called the plastic strain ratio, is a measure of the normal anisotropy of sheet materials; it will now be discussed below.

R is most frequently measured by the average plastic strain ratio, \bar{R} , which is defined as:

$$\bar{R} = \frac{r_0 + 2r_{45} + r_{90}}{4} \quad (2.3)$$

where 0, 45, and 90 are the inclinations of the tensile specimen axis with respect to the rolling direction in degrees. If $r_0 = r_{45} = r_{90}$, $\bar{R}=1$, indicating isotropy. As a preferred orientation, or texture, is developed, the value of \bar{R} changes. A metal with an \bar{R} value greater than one will

exhibit better deep drawability than a completely isotropic one. In general, the higher the \bar{R} value, the better the formability.

The importance of texture in the final application of this work, therefore, is more complicated than just the development of dynamic recrystallization and its inherent texture. The final texture must also have a favorable \bar{R} value to be desirable.

2.7 Texture

In the solid state, metals consist of atoms organized in specific crystalline patterns. However, metals are not typically single crystals, but occur in polycrystalline aggregates. This, in effect, means the metal is composed of many different crystals. Each crystal has a specific, and usually unique, orientation relative to some reference. However, this does not mean that the crystals, or grains, are randomly oriented. While a completely random orientation is possible, usually this is not the case. During plastic deformation, the crystals tend to rotate to specific stable orientations. These stable or 'preferred' orientations are known as textures. In addition, when metals recrystallize, new grains of certain orientations preferentially grow into the deformed crystals. This replaces the previous 'deformation' texture with another, a 'recrystallization' texture.

Recovery does not have a drastic effect on texture as the resulting orientation usually only varies slightly from the deformation texture. The texture present in the material is important as most physical and mechanical properties of a metal are dependent on the orientations of the crystals. This means that a metal with a certain texture will exhibit a particular kind of anisotropy. The forming operations associated with the automotive

applications of IF ferritic stainless steels depend on this anisotropy for successful deep drawing, as discussed above [18,57].

2.7.1 Texture Representations

The basic representation of texture is the pole figure. This is essentially a stereographic projection showing the distribution of a set of poles described by Miller indices $\{hkl\}$ in orientation space. Each crystal has a pole or orientation. A completely random texture would be represented by a uniform intensity of poles. If a metal has a strong texture, this would be shown by a tight cluster of poles in certain orientations. Since textures in most polycrystalline metals can be quite complex, often one or two additional pole figures determined for other crystallographic reflecting planes are used for comparison so the relative intensities of orientations are obvious.

A more complex, but more instructive representation for texture commonly used today is the Orientation Distribution Function (ODF). To summarize the principles of this method, it is necessary to describe Euler angles. Like the pole figure, this is a way of specifying an orientation with respect to an external reference frame. Basically, this is a relation between the orientation of the crystal and the orientation of the sample. The orientation of the crystal can be transformed into the orientation of the sample by rotation. This is composed of three consecutive rotations $g_{\phi 1}$, g_{ϕ} , and $g_{\phi 2}$. The ODF is a representation of the volume of elements (crystals) that possess the orientation g as compared to the total volume. A random texture would have an ODF value of 1 whereas a typical ODF value would range from 2 to 100, where 2 is a weakly textured and 100 is a strongly textured polycrystal [58].

Chapter III

EXPERIMENTAL PROCEDURE

3.0 Background

Previous to this work, the general dynamic softening behavior of ferritic stainless steels in general and the torsion behavior in particular was unknown. This work provides insight into the evolution of torsion textures in two interstitial-free ferritic stainless steels over a range of strains and temperatures. The torsion test was chosen for this project due to the large strains possible. In addition, the computer control of the deformation process with the torsion machine is much more precise. Determination of the softening kinetics was performed so as to avoid the occurrence of postdynamic or static recrystallization. Finally, the deformed specimens were analyzed using texture measurement and microstructural analysis.

3.1 Materials

The chemical compositions of the steels investigated in this work are given in Table III.1. These steels were kindly provided by Armco Research in the form of 13 mm thick hot rolled plates.

Table 3.1 Chemical compositions of the experimental materials

Stainless Steel	C	N	Nb	Ti	Cr
IF Ti Stab.	0.002	0.005	<0.01	0.23	11.1
IF Ti & Nb Stab	0.003	0.004	0.1	0.09	11.1

with: 0.5% Si, 0.2% Ni, 0.04% Mo, 0.02% P, 0.003% S, 0.3% Mn, 0.06% Cu, 0.01% Al

Torsion samples were prepared from these steels in such a manner that the sample axis corresponds to 1/4 of the slab thickness. Solid bar specimens were used for these experiments, with a diameter of 6.3 mm and a gauge length of 22.2 mm. The geometry of these samples is shown in Fig. 3.1.

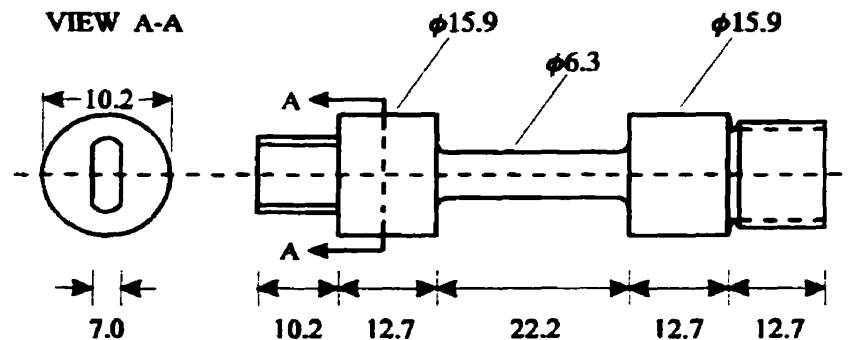


Figure 3.1 Schematic of torsion test sample [39].

3.2 Torsion Testing

The torsion tests were performed on a servo-hydraulic machine controlled by an MTS system. The test data, twist, temperature, time, and torque data were acquired by computer. The torsion machine, which is

mounted on a lathe bed, is powered by a hydraulic servovalve, Fig. 3.2, which controls the flow of oil to a hydraulic motor. The rotational force is transmitted by the rotating torsion anvil and the rotational displacement is measured by a 50-turn potentiometer, the limit on this particular machine. The sample is mounted by screwing the threaded end into the stationary anvil connected to the torque cell, while the other end of the sample is fitted into the slot in the rotating anvil. To allow for the thermal expansion involved in high temperature tests, a gap of about 2 mm was always left between the specimen and shoulder of the rotating grip. The applied torque was measured by a 112.98 N-m (1000 in-lb_r.) torque cell. A more detailed description of the torsion machine is given in the literature [59].

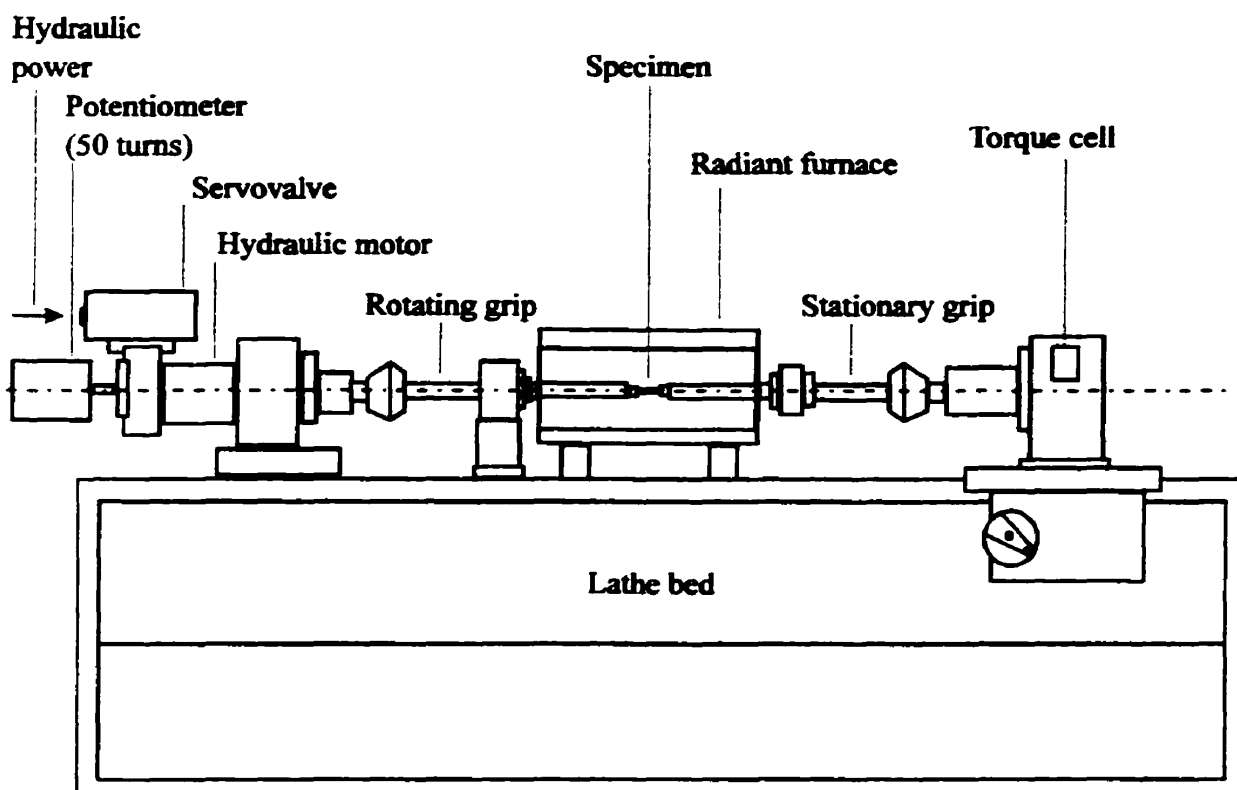


Figure 3.2 Schematic of torsion test equipment [39].

Chapter III Experimental Procedure

The sample was heated by a four element radiant furnace manufactured by Research Incorporated with the temperature controlled by a K type thermocouple which was in contact with the gage length of the specimen. High purity argon was circulated through a quartz tube encompassing the sample and anvils to minimize oxidation during the high temperature tests. An Electromax process controller coupled to a Leeds and Northrop 1300 process programmer regulated the temperature during the test. The Leeds and Northrop 1300 both displayed the temperature and sent the analog signal to the TestStar workstation interface (MTS System Corp.) controlling the torsion machine.

The TestStar workstation interface was connected to a torque control panel and to a 486 generation PC running the TestStar software under the OS/2 operating system. The twist-temperature-time-torque data acquired by the computer were saved as an Excel 5.0 file in a form suitable for further calculations and for graphical presentation.

The various torsion tests performed both to determine the optimum conditions for the investigation of dynamic recrystallization in the ferrite range and to generate the actual textures are detailed below.

3.2.1 Softening Behavior Characterization

The softening kinetics were measured at 1000°C. Previous work [60] indicated that testing must be done at a low strain rate if static recrystallization is to be avoided in the interval before quenching after the test. As in the work by Baczynski, a strain rate of 0.1 s^{-1} was used. Double twist tests were carried out, Fig. 3.3, to determine the softening kinetics of the steels. Two series of softening tests were performed, one near the 'peak' strain and one close to fracture. The sample was deformed

to the point in question, held at a constant temperature for a certain period of time, then deformed again. The times held were based on a logarithmic scale ranging from nearly 2 to 1000 seconds. The percentage of softening was calculated as the ratio: $(\sigma_M - \sigma_1) / (\sigma_M - \sigma_0) \times 100$, where σ_M is the flow stress at interruption and σ_0 and σ_1 are the 0.2% offset stresses in the first and second twists, respectively. In order to be as precise as possible, the stress values were taken directly from the data files and plotted in the form of softening versus holding time diagrams.

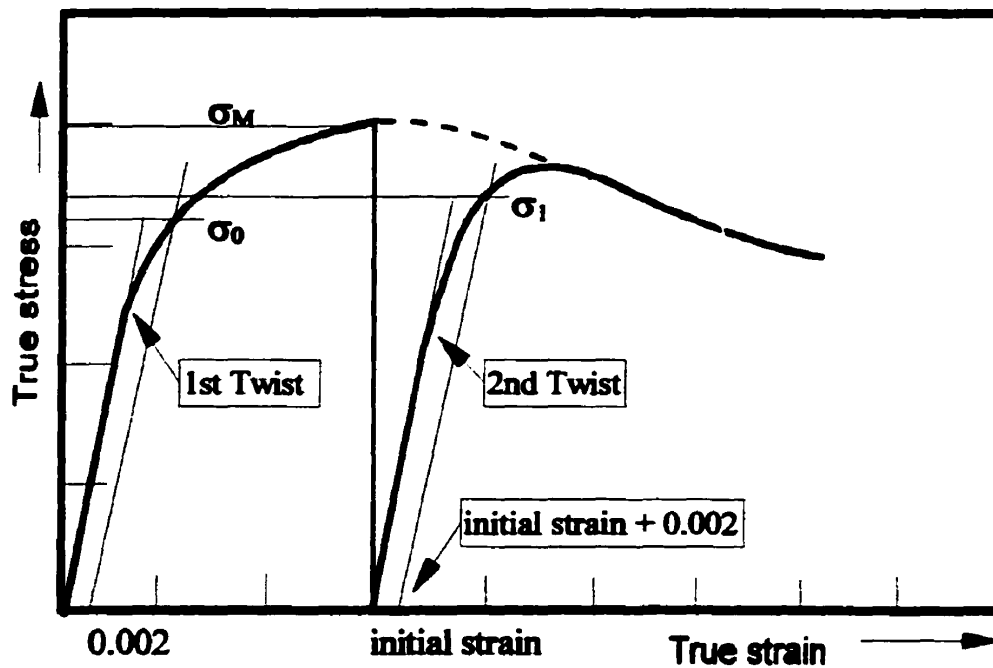


Figure 3.3 Schematic representation of the 0.2% offset method for calculating the softening kinetics [39].

3.2.2 Continuous Torsion Tests

Continuous torsion tests were performed at both room temperature and elevated temperatures. Both the twist, θ , and the twist rate, $\dot{\theta}$, were regulated using the TestStar program so that they corresponded to the applied strain, ϵ , and strain rate, $\dot{\epsilon}$. The relationships between these values are as follows [61-63]:

$$\gamma=r\theta/L, \quad \dot{\gamma}=r\dot{\theta}/L \quad (3.1)$$

$$\theta=\gamma L/r \quad (3.2)$$

$$\epsilon=\gamma/\sqrt{3}, \quad \sigma=\sqrt{3}\tau \quad (3.3)$$

where γ is the shear strain;

$\dot{\gamma}$ is the shear strain rate;

r is the radius of the sample;

L is the gage length;

ϵ is the von Mises equivalent strain;

σ is the von Mises equivalent stress;

τ is the shear stress.

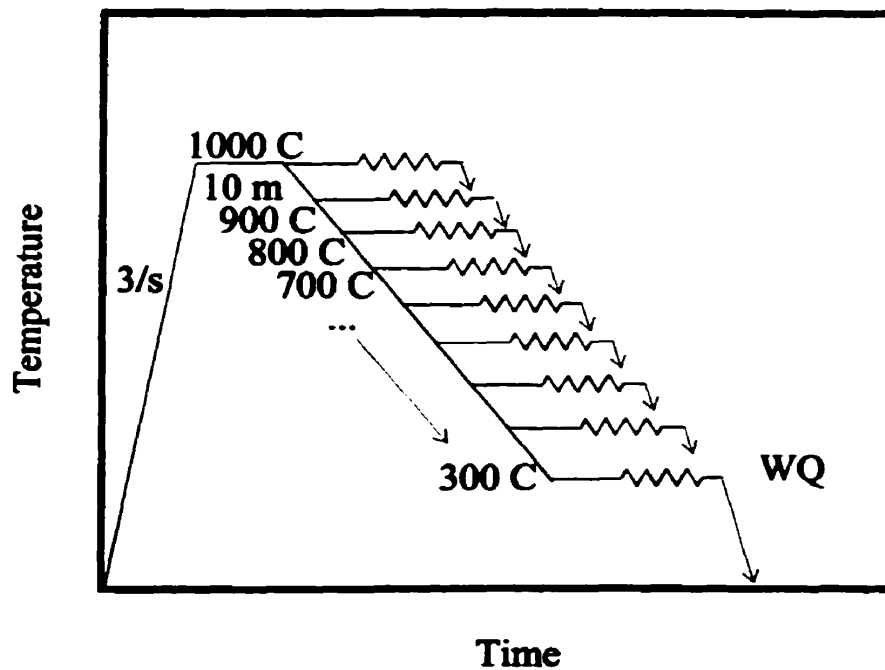
The Fields and Backofen [63] equation was used to determine the von Mises equivalent stress σ :

$$\sigma=\frac{\sqrt{3}T}{2\pi r^3}(3+m+n) \quad (3.4)$$

where T represents the developed torque, m is the macroscopic strain rate sensitivity and n is the macroscopic strain hardening coefficient. For these experiments, the m and n parameters were taken to be constant at values of 0.17 and 0.13, respectively.

Chapter III Experimental Procedure

The thermomechanical schedule of the samples deformed at or below 1000°C is shown in Figure 3.4. This schedule was used to simulate the industrial conditions. The samples were heated to 1000°C at a rate of 3°C/s and held at that temperature for 10 minutes to achieve equilibrium conditions. The samples were then cooled (if necessary) at a rate of 1°C/s to the temperature of deformation. The samples were then held for 5 minutes, again to achieve equilibrium. At this point, the samples were deformed and, except for room temperature deformation, quenched in a water bath in order to retain the as hot deformed structure and texture. The delay between the end of the test and the quench ranged from 2 to 4 seconds, resulting from the time required to remove the sample from the furnace and apply the water quench.



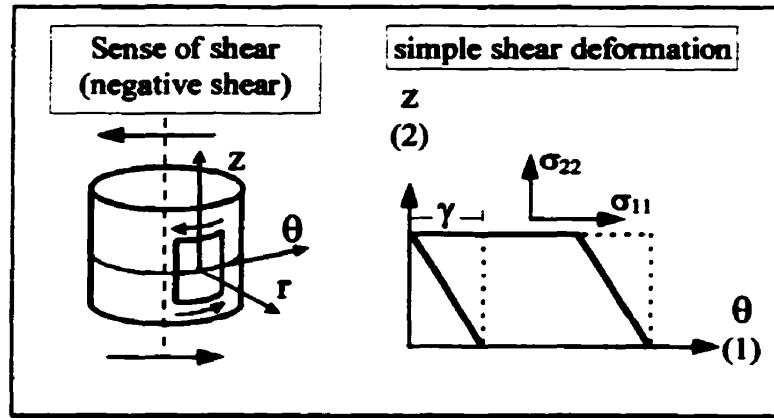
3.4 Test schedule for torsion samples.

Chapter III Experimental Procedure

For the samples deformed above 1000°C, the same process was followed except that the sample was heated directly to the deformation temperature.

3.3 Texture Sample Preparation

The deformed torsion samples were prepared for texture measurement as shown in Fig. 3.5. The specimen gauge length was drilled out in order to produce a hollow cylinder with a wall thickness of about 0.4 mm. The sample was then chemically polished in a solution of half hydrofluoric acid and half hydrogen peroxide for about 2 minutes in order to thin the wall of the cylinder. The outside surface was covered with tape so the inside surface would be preferentially attacked. The tube was cut on one side along the axis and carefully opened and flattened. The additional strain imposed by this operation was estimated at less than 0.06, which was not expected to affect the final texture. The samples were then polished using standard metallographic techniques. First, rough polishing was performed using silicon carbide paper with an ascending grit number. Next, the sample was fine polished using 6 μm diamond paste and 0.5 μm alumina powder suspension. Then etching was performed for metallographic reasons. Finally, the samples were chemically polished again to remove some of the deformation of mechanical polishing, as electropolishing was not possible.



Figures 3.5 (left) Sample reference system in torsion & 3.6 the pole figures are oriented with respect to the θ , z , and r axes of the sample [39].

3.4 Metallographic Analysis

Metallographic analysis was performed before chemical polishing. The samples were etched in a three to one mixture of hydrogen peroxide and HF [64]. The samples were examined using a LECO image analysis system and microscope. Several micrographs were taken during examination to provide illustration of the representative microstructures. In some cases, the average grain size was estimated using the standard linear intercept techniques.

3.5 Texture Measurement

The $\{110\}$, $\{200\}$, and $\{211\}$ incomplete pole figures were measured on a Siemens D-500 goniometer system. The orientation of the (θ, z, r) reference frame used in this thesis is shown in Fig.3.6 (above). and is

related to the sample axes. The method of texture measurement employed in this work involved generating negative shear in the torsion sample. The apparent sense of this shear is reversed when the reflection method is applied to the inner as opposed to the outer surface of the specimen, or when the goniometer moves clockwise as opposed to counterclockwise while collecting data. Extreme care was taken to ensure these effects did not affect the pole figures and ODFs.

The series expansion method introduced by Bunge [58] and discussed in detail by Van Houtte et al. [65] for the case of monoclinic sample symmetry was used in the present work. ODFs were calculated on the basis of cubic crystal and monoclinic sample symmetry from the {110}, {200}, and {211} incomplete pole figures.

Chapter IV

Experimental Results

4.1 Softening Kinetics

The softening kinetics were determined as described above. A series of these tests were performed at 900°C and some tests at 1000°C using a range of hold times for both materials. The results from the softening tests are compiled in Figs.4.1 and 4.2. The temperature, strain rate, and initial strain are indicated in Figs. 4.1 and 4.2.

The titanium stabilized stainless steel showed very little softening at holding times below 100 s. The amount of softening drastically increases until a nearly fully restored flow stress is reached around 1000 s. In the titanium-niobium stabilized stainless steel, softening did not occur to a large extent at the lower holding times. Even at the longer holding times, the total softening did not reach 50%.

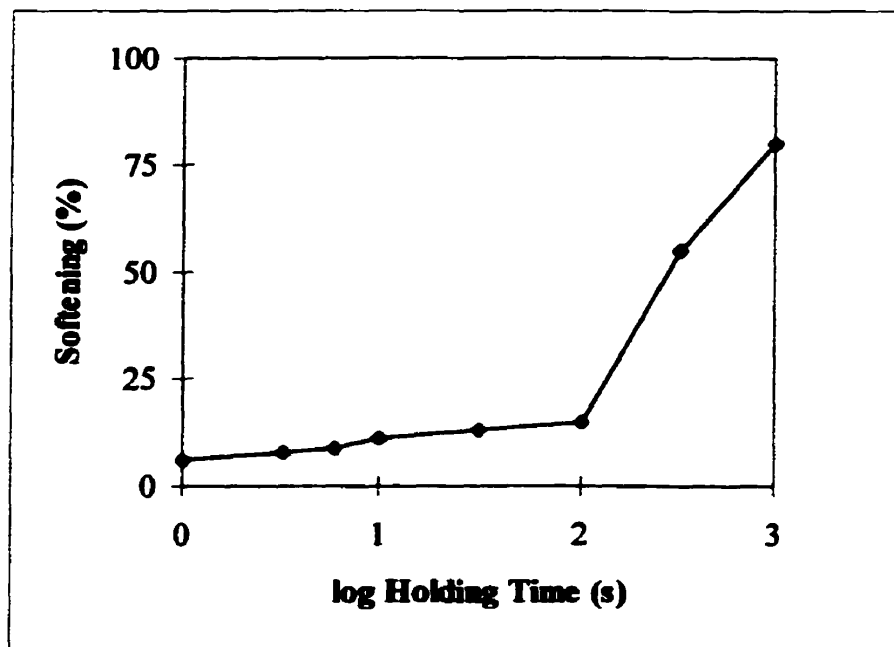


Figure 4.1 Softening curve of Ti IF 409.

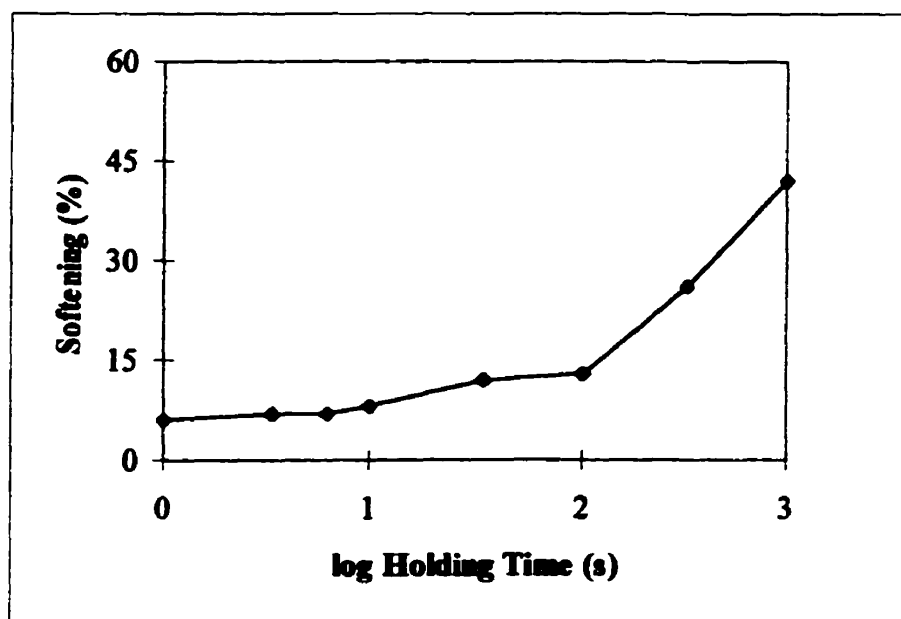


Figure 4.2 Softening curve of Ti-Nb IF 409.

4.2 Flow Curves

Both materials displayed similar flow curves when deformed at room temperature at a strain rate of 0.1 s^{-1} , Fig. 4.3. The titanium stabilized steel exhibited a slightly lower strength and fractured at a slightly lower strain.

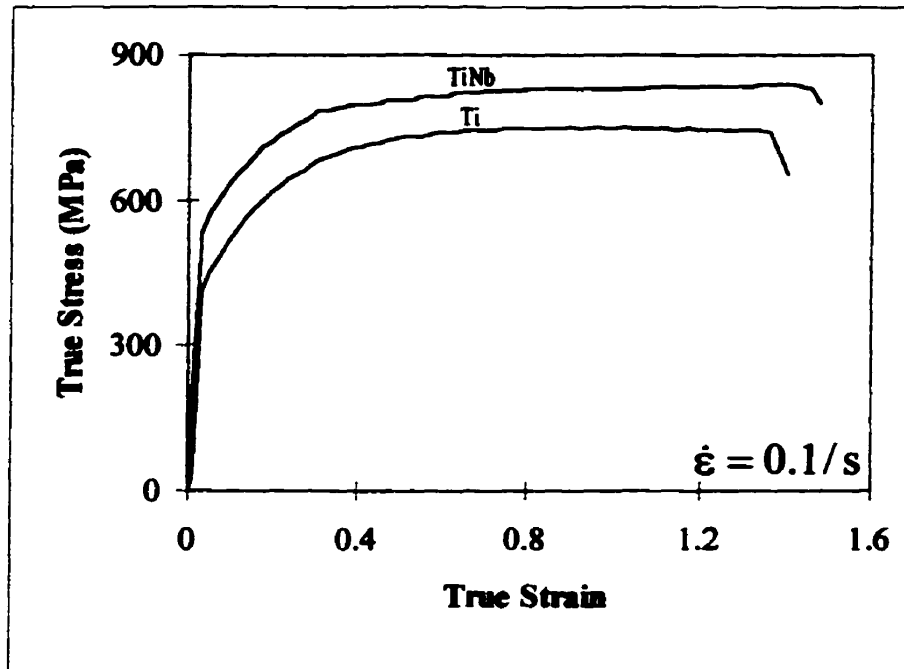


Figure 4.3 Both steels deformed at room temperature.

The true stress-true strain curves for the titanium stabilized stainless steels deformed at elevated temperatures are shown in Fig. 4.4. These curves show a common pattern. First, none of the curves exhibit a definite maximum stress or 'peak'. Second, the steady state region is reached at lower strains as the temperature of deformation increases. The sample deformed at 700°C fractured at a strain of about 4, before the 'steady state' was reached. However, due to the small amount of work hardening in ferritic metals, this behavior is not really indicative of the presence of significant amounts of softening. In contrast, the specimens deformed

above 700°C did not fracture, even when deformed to large strains approaching 14-15.

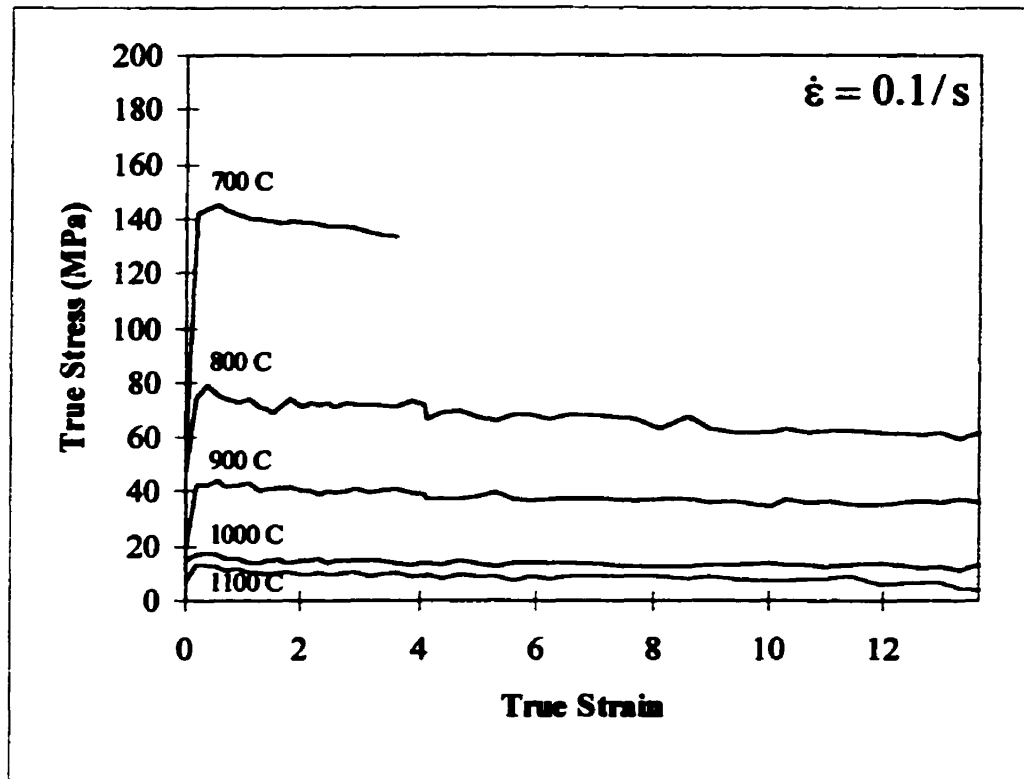


Figure 4.4 Flow curves of Ti IF 409 at various temperatures.

As with the room temperature deformation, the titanium-niobium stabilized steels behaved in a similar manner, Fig 4.5. At 700°C, the specimen fractured at a strain of nearly 2. Above this temperature, a large 'steady state' region is observable. The specimens deformed at 800 and 900°C fractured before a strain of 14, while the specimens deformed above these temperatures did not fracture at strains approaching 15.

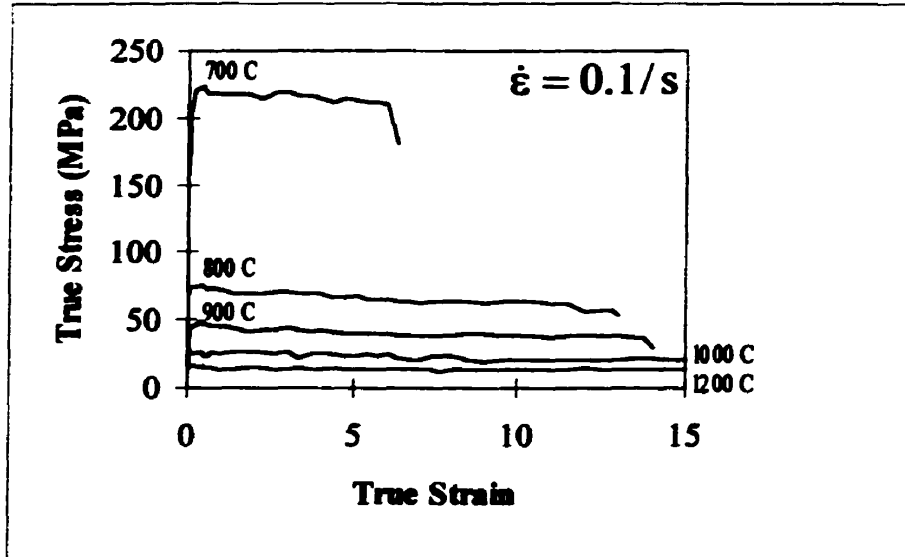


Figure 4.5 TiNb IF 409 deformed at various temperatures.

4.3 Microstructural Observations

The initial grain size of the titanium stabilized stainless steel was estimated to be approximately $190 \mu\text{m}$, Fig 4.6a. The grains are irregularly shaped and seem to be of a fairly uniform size. After room temperature deformation, the microstructure changed considerably, Fig 4.6b. The grains become quite elongated at angles of β° with respect to the shear direction, which is shown in the micrograph. The torsion axis, z , is directed upward and lies in the plane of the micrograph. The angle β decreases with increasing strain to about 20° at a strain of 1.4, as per the formula $\tan 2\beta = 2/\gamma$ determined by Canova *et al.* [61]. This deformation-induced microstructure is also present as the temperature is increased, Fig. 4.6c. At the temperature at which dynamic recrystallization is reached, a new structure emerges Fig 4.6d. The dynamic recrystallization microstructure is finer ($\sim 50 \mu\text{m}$) and more equiaxed.

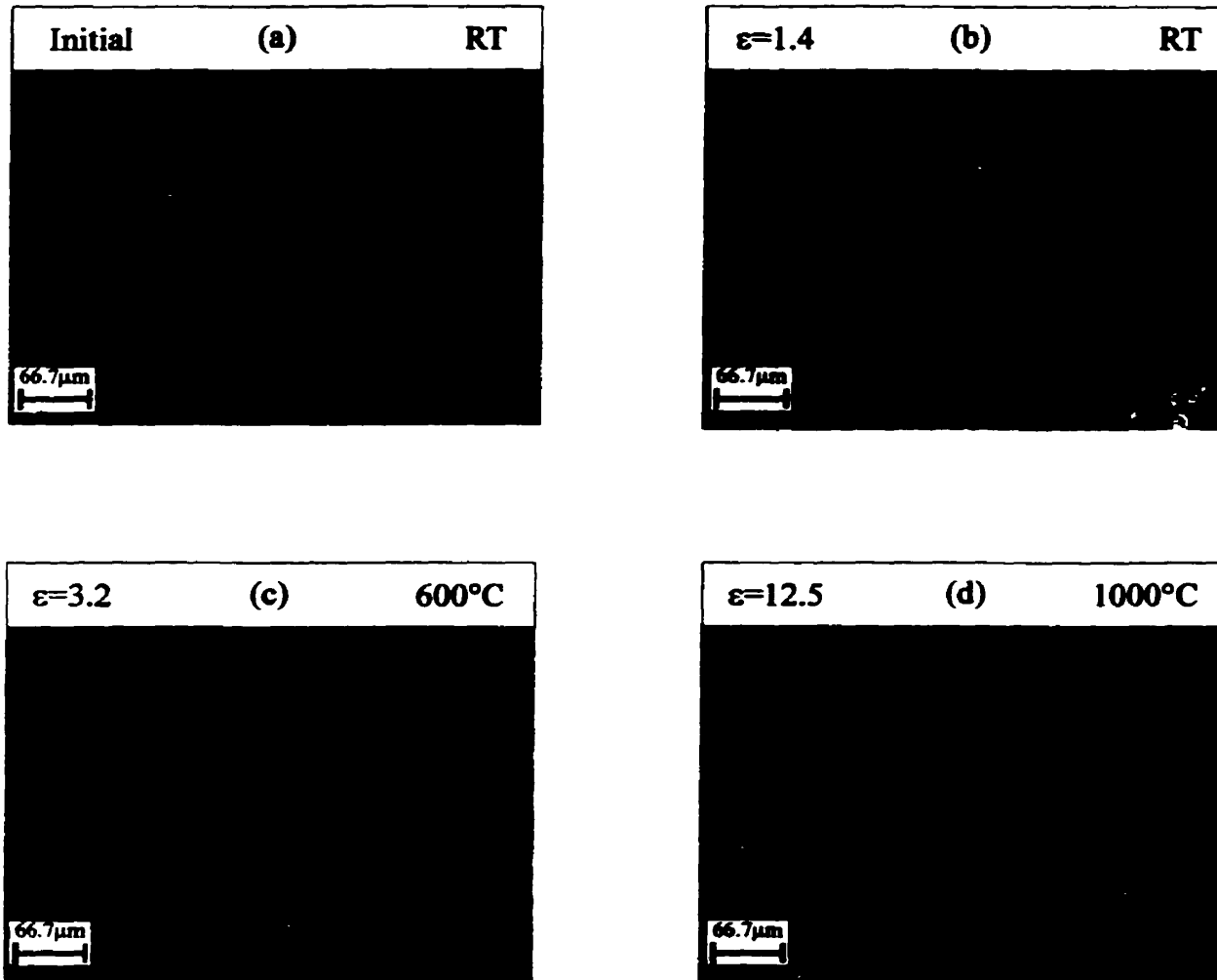


Figure 4.6 Microstructures of Ti IF 409.

The titanium-niobium stabilized steel, again, behaved in a manner similar to that of the titanium stabilized steel. The starting microstructure had a slightly smaller grain size, approximately 155 μm , but was relatively equiaxed, Fig.4.7a. The microstructure after room temperature deformation was highly elongated at an angle of about 20°, Fig.4.7b. Again, the room temperature deformation structure continues to appear in the low temperature specimens ($<T_{\text{rns}}$), Fig.4.7c. Fig 4.7d illustrates the structure found in the samples deformed above the recrystallization temperature. As with the titanium stabilized steel, the grain size is finer ($\sim 25 \mu\text{m}$) than that of the lower temperature specimens and a more equiaxed structure is evident. In addition, the degree of refinement due to recrystallization is higher in the titanium-niobium stabilized steel.

4.4 Texture Measurements

The test matrix for texture measurement is shown in Table 4.1. The von Mises equivalent strains listed in the tables were corrected for the presence of the radial strain gradients. The correction is required because the radius of the samples was reduced during preparation for texture measurement, a procedure that was described in section 3.3. In addition, the 'final' textures are from samples which were not deformed to fracture, but to a slightly lower strain for obvious reasons.

To aid in analyzing the texture results, some important ideal orientations are listed in Table 4.2. These orientations are specified in terms of the shear plane (SP) and shear direction (SD) as well as the relevant Euler angles (ϕ_1, Φ, ϕ_2) in the Bunge notation.

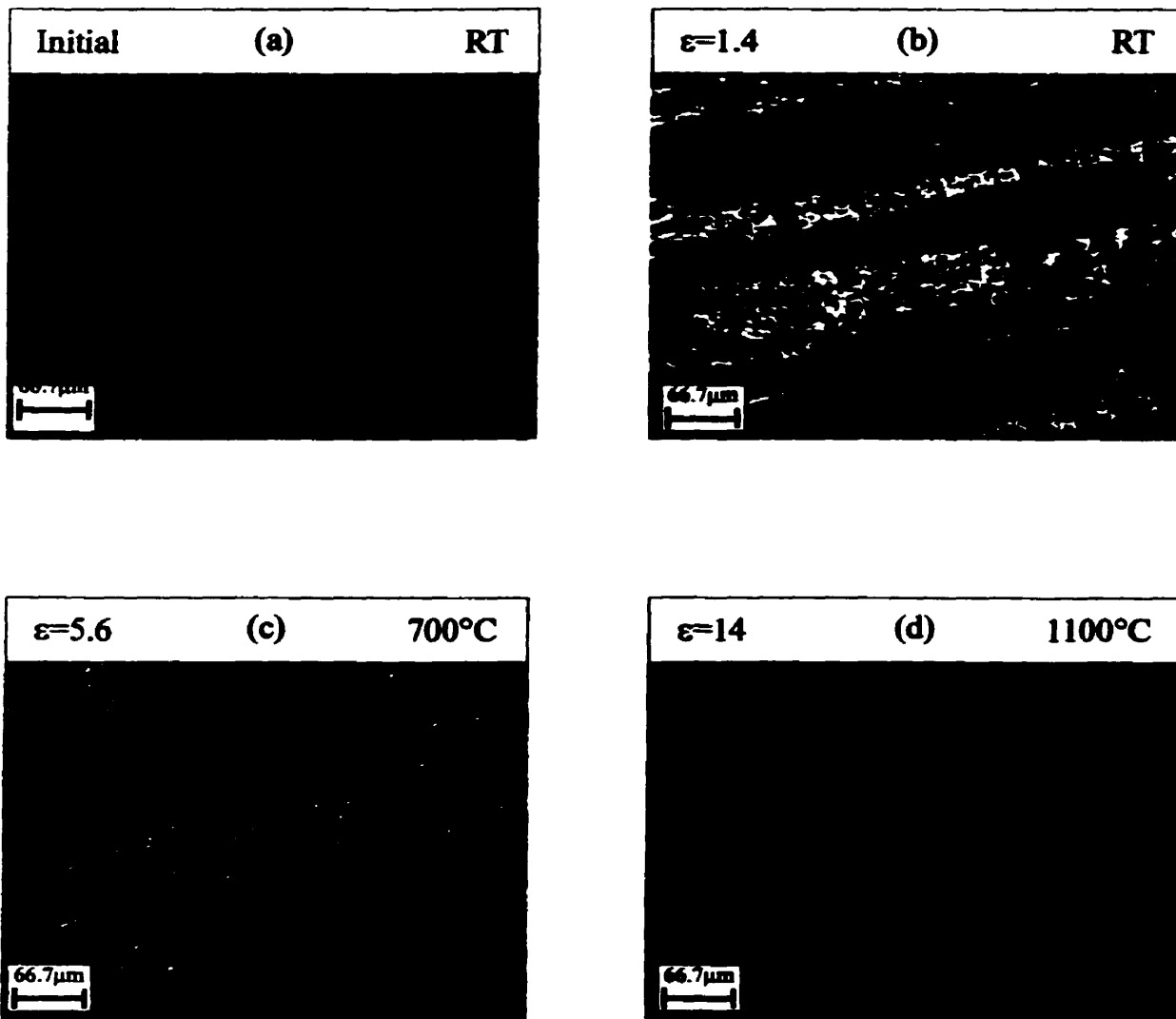


Figure 4.7 Microstructures of TiNb IF 409.

Table 4.1 Test Matrix

Steel	Temp, °C	$\epsilon \approx \text{low}$	$\epsilon \approx \text{high}$
Ti IF 409	RT		1.35
	400		2.6
	500		2.8
	600		3.2
	700		5.5
	800	7.9	13.3
	900	8.0	13.4
	1000	7.9	13.4
	1100	7.9	13.3
Ti-Nb IF 409	RT		1.3
	700		5.6
	800		12.0
	900		13.4
	1000		13.5
	1100		13.4
	1200		13.6

Table 4.2 Some important torsion ideal orientations

Orientation	SP	SD	ϕ_1	Φ	ϕ_2
F	(110)	[001]	180.0	45.0	0.0
D1	(11 $\bar{2}$)	[111]	125.3	45.0	0.0
D2	($\bar{1}$ 12)	[111]	54.7	45.0	0.0
E1	(01 $\bar{1}$)	[111]	39.2	65.9	26.6
E2	(0 $\bar{1}$ 1)	[111]	90.0	35.3	45.0
J1	(0 $\bar{1}$ 1)	[$\bar{2}$ 11]	30.0	54.7	45.0
J2	(1 $\bar{1}$ 0)	[$\bar{1}$ 12]	150.0	54.7	45.0

The $\{110\}$ pole figure for these ideal orientations is shown in Fig. 4.8. They form two types of fibers: the $\{110\}\langle uvw \rangle$ results from rotation of a $\{110\}$ plane (shear plane) around the z axis, and the $\{hkl\}\langle 111 \rangle$ originates from a rotation of a $\langle 111 \rangle$ direction around the θ axis. Some important texture components not reported previous to the work of Baczynski [39] are identified here as J1 and J2.

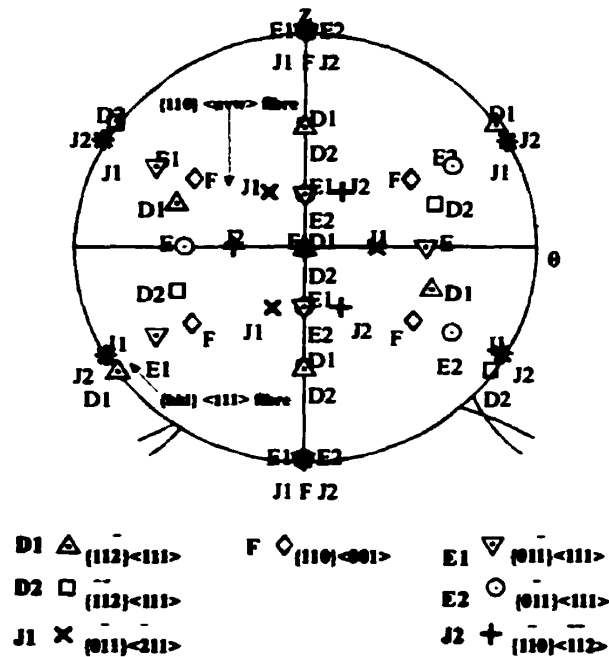


Figure 4.8 $\{110\}$ pole figure displaying the ideal orientations observed during the present torsion tests.

The results of the ODF analyses are listed in Tables 4.3 and 4.4 and Figs. 4.9-4.28. For ease of analysis, the f_1 , f_2 , and f_3 torsion fibers and the ideal orientations of Table 4.2 are identified. All tests were performed at a strain rate of $\dot{\epsilon} = 0.1/s$.

Chapter IV Experimental Results

For the ODFs, the three dimensional space is represented by a series of 'slices'. On each, the ϕ_1 angle runs across the x-axis of the ODF from 0 to 180° (left to right). The Φ angle runs along each section of the ODF from 0 to 90° (top to bottom). The ϕ_2 angle is represented by the sectioning of the ODF every 15° from 0 to 90°. The $\phi_2=0^\circ$ is the top section, while the second is the $\phi_2=15^\circ$ and the bottom section is $\phi_2=90^\circ$. In other words, the horizontal axis in any section is the ϕ_1 , the vertical axis in any section is the Φ , and the vertical (out of the page) axis is represented by the ϕ_2 sections.

Table 4.3 Experimental ODF intensities for some important orientations in the Ti stabilized IF 409

Temp	RT	400	500	600	700	800	
Strain	1.35	2.6	2.8	3.2	5.5	7.9	13.3
J	2.2	5.3	5.7	3.1	4.2	4.6	4.3
F	5.6	2.6	3.0	3.9	5.8	4.6	1.7
D1	3.5	3.0	4.9	6.2	6.9	4.9	3.0
D2	0.0	2.0	1.8	3.4	3.0	3.2	20.1
E1/E2	3.4	3.4	2.9	3.1	9.5	3.6	4.7
Temp	900		1000		1100		
Strain	8.0	13.4	7.9	13.4	7.9	13.3	
J	4.4	1.8	3.3	1.2	0.9	0.9	
F	2.7	2.7	1.1	0.4	1.7	2.0	
D1	5.0	5.7	1.9	9.6	8.2	7.8	
D2	5.4	16.2	8.0	44.8	54.0	71.1	
E1/E2	3.6	1.4	1.6	1.4	0.8	1.4	

Table 4.4 Experimental ODF intensities for some important orientations in the Ti-Nb stabilized IF 409

Temp	RT	700	800	900	1000	1100	1200
Strain	1.3	5.6	12.0	13.4	13.5	13.4	13.6
J	3.6	4.7	2.0	1.1	2.4	0.1	1.1
F	3.1	2.7	1.35	0.5	3.9	0.1	0.1
D1	7.0	3.7	5.1	6.7	2.9	6.4	16.0
D2	3.9	4.8	7.0	9.9	11.0	27.8	38.7
E1/E2	4.8	3.5	4.8	4.8	1.4	0.7	0.6

The room temperature deformation textures are shown in Figs. 4.9 and 4.10. Examination of the ODFs shows that the preferred orientations lie upon the f_1 , f_2 , and f_3 fibers. In addition, the orientations are slightly shifted in the increasing PHI1 (ϕ_1) direction from their symmetrical positions. In the titanium stabilized steel, the texture consists of the components F $\{110\}\langle 001\rangle$, E $\{001\}\langle 111\rangle$, J $\{110\}\langle 211\rangle$, and D $\{112\}\langle 111\rangle$, listed in order of decreasing importance, although the values are not very different. For the titanium-niobium stabilized steel, the results were similar. The final texture consists of the components D, E, J, and F, again listed in order of decreasing importance. The magnitude of the D1 component was a bit surprising in comparison to that of the other components.

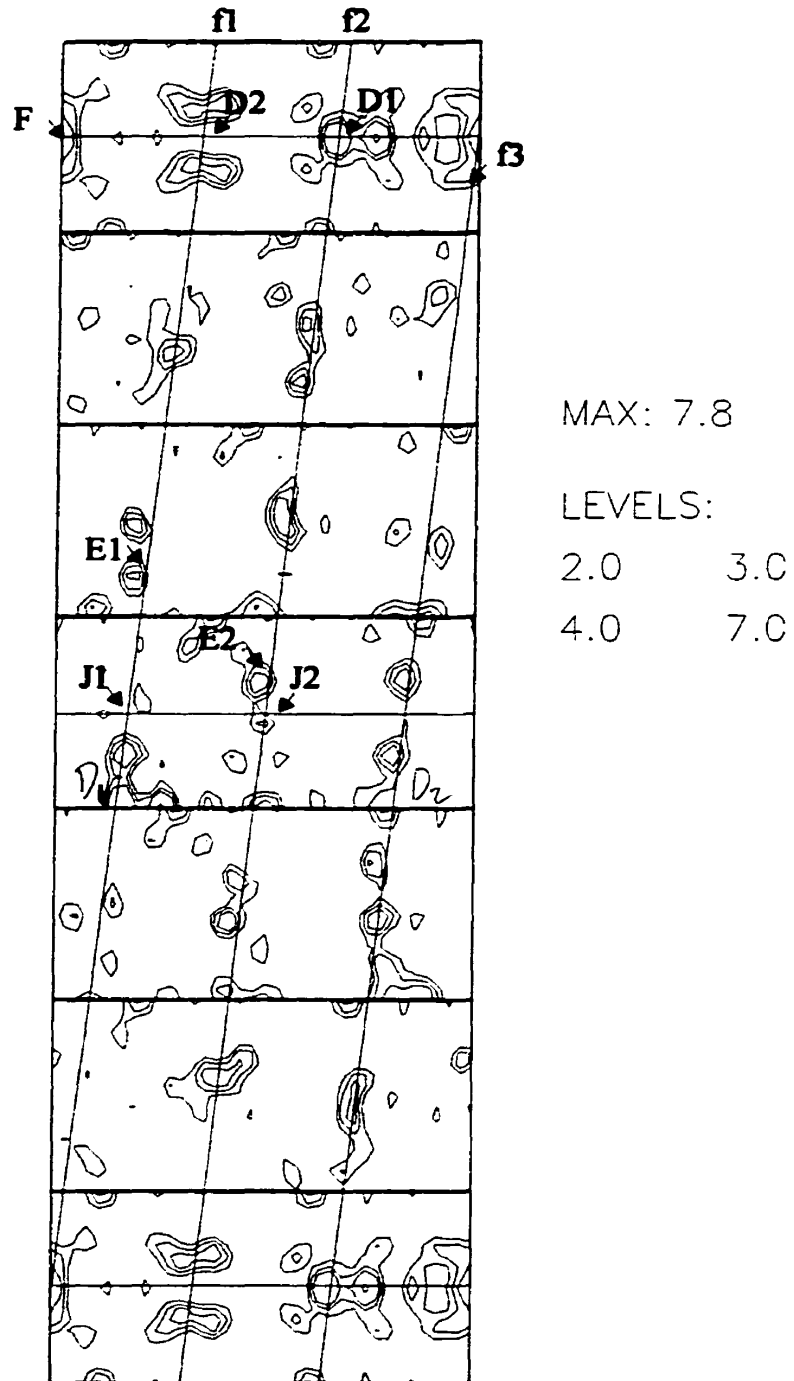


Figure 4.9 Ti IF 409 deformed at RT.

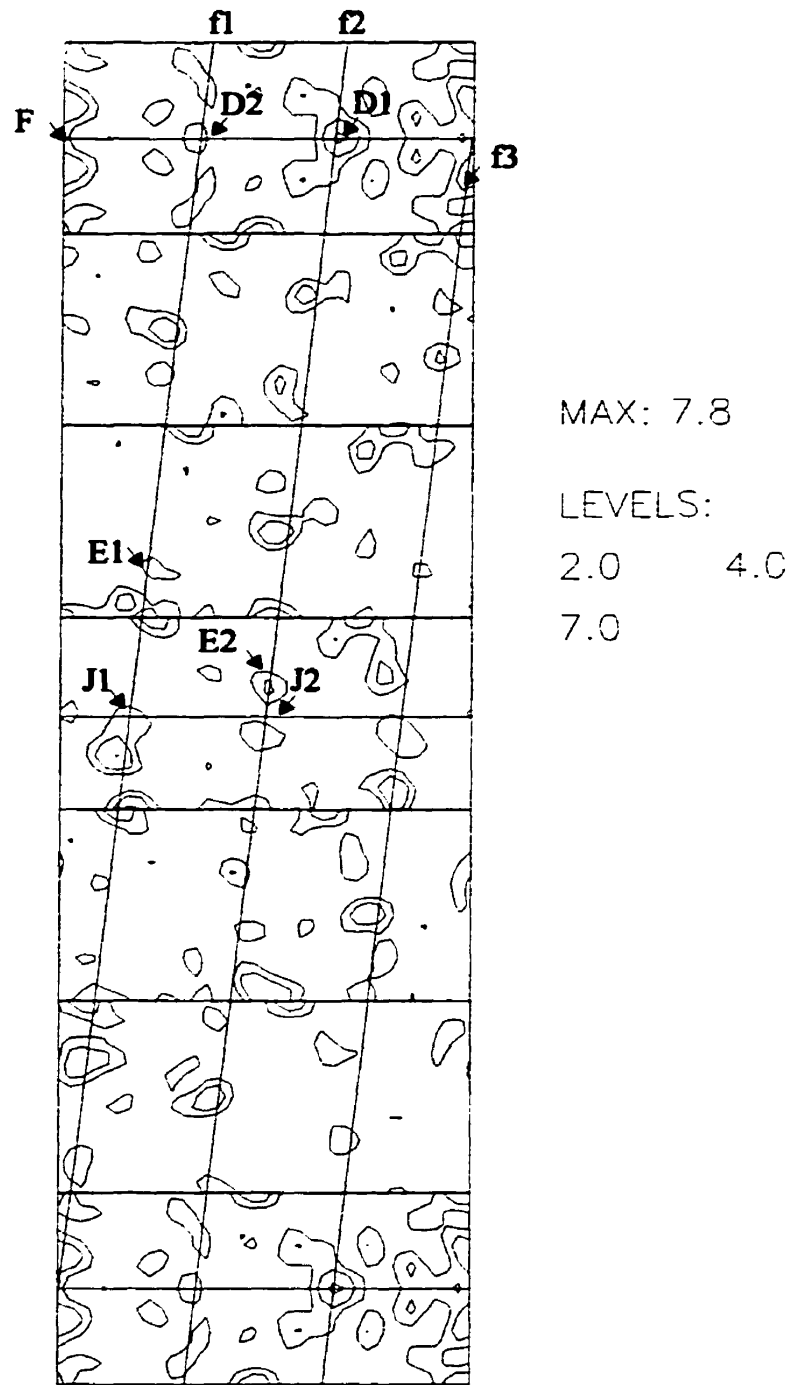


Figure 4.10 TiNb IF 409 deformed at RT.

The textures for the titanium stabilized steel deformed between 400 and 700°C are shown in Figs.4.11-4.14. It should be noted that the orientations along $\Phi=90^\circ$ in the $\varphi_2=45^\circ$ section are the symmetrical equivalents of those located along $\Phi=45^\circ$ in the $\varphi_2=0^\circ$ section. The fibers and maximum intensities are similar to those of the room temperature texture. The textures of the specimens deformed at 600 and 700°C begin to show a change in the importance of the various intensities. This will be discussed later. In any case, the textures do show a common pattern and a few differences. The J and F components are important in all these samples as well as in the room temperature texture. J and F result from room temperature dislocation glide. As the temperature increases, the D1/D2 and E1/E2 components become more important as well. One important aspect is the marked increase of the E1/E2 component at 700°C, suggesting that this texture is in transition to a higher temperature one.

Chapter IV Experimental Results

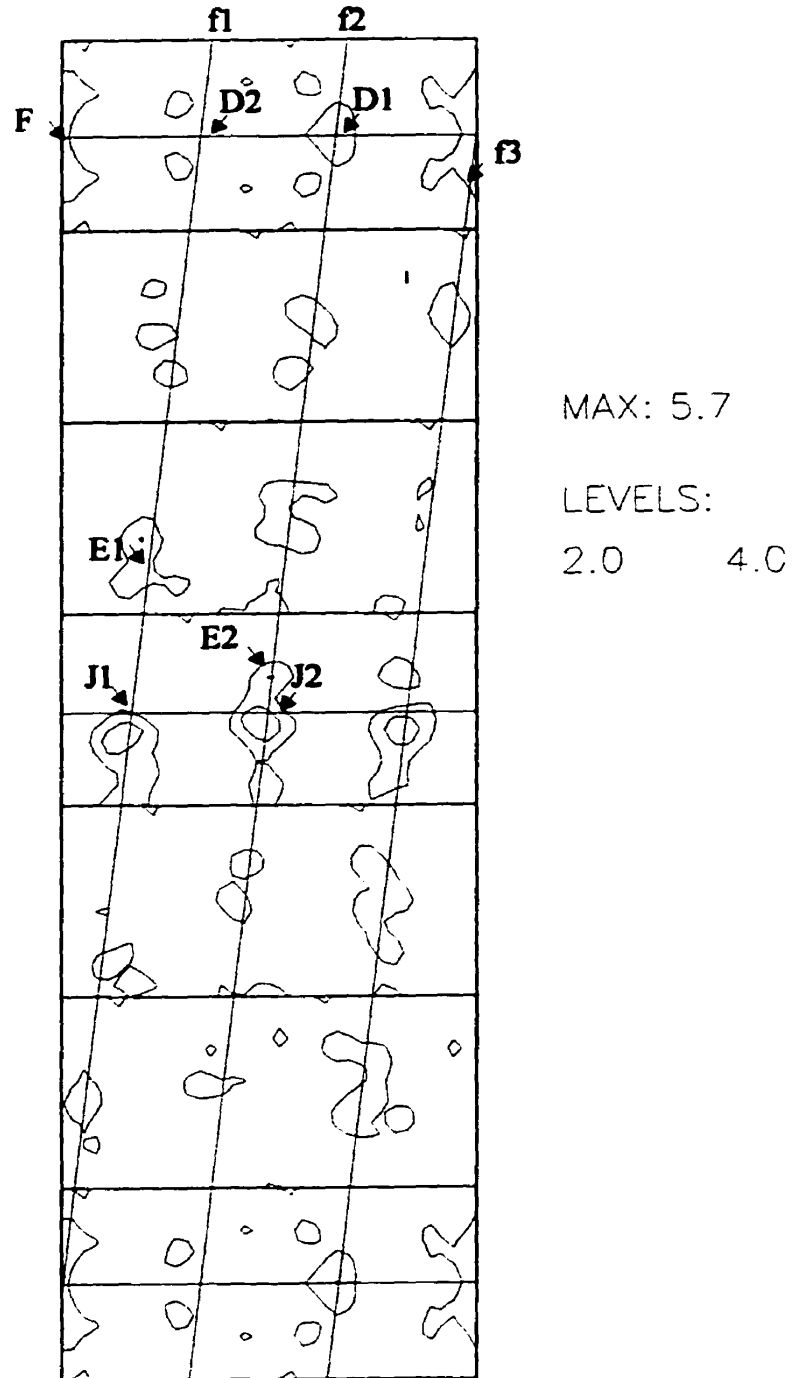


Figure 4.11 Ti IF 409 deformed at 400 C.

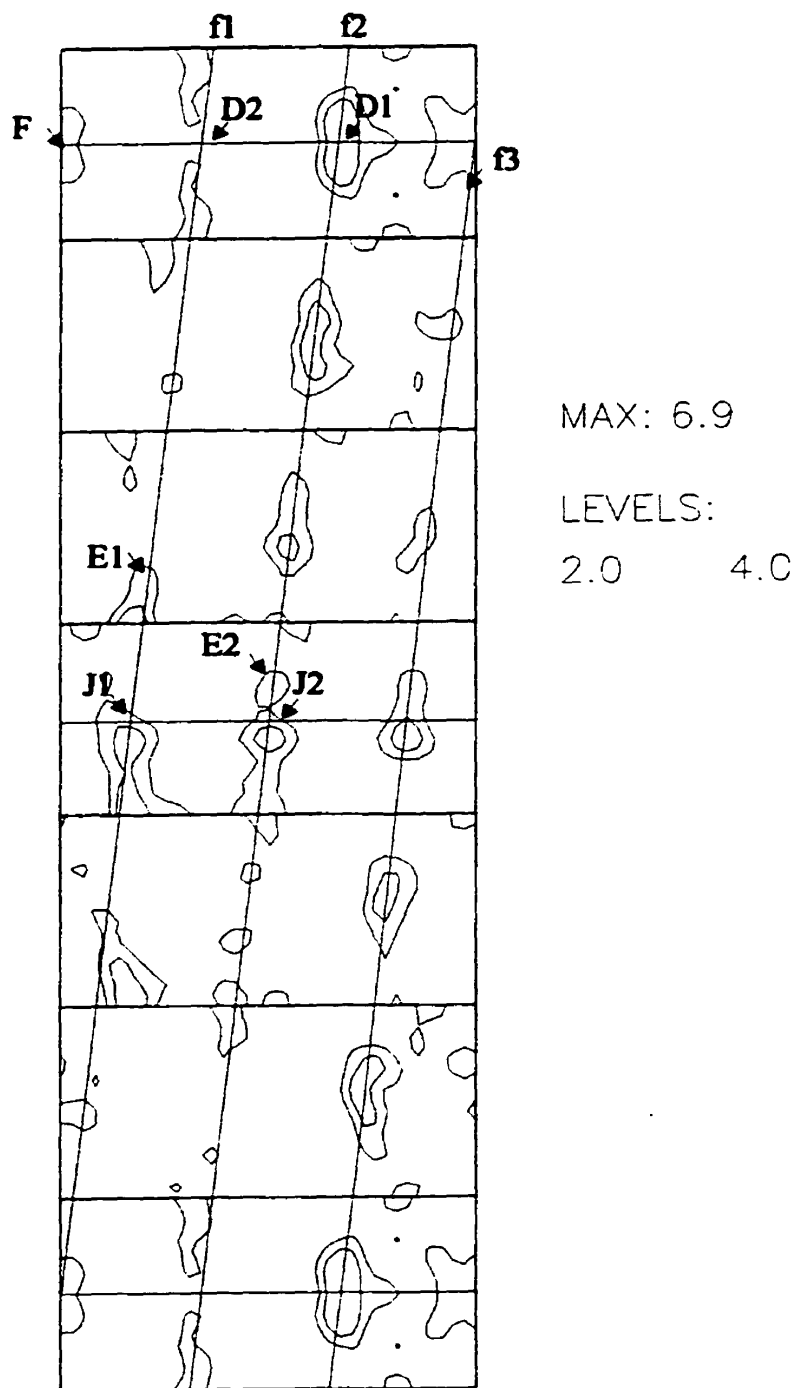


Figure 4.12 Ti IF 409 deformed at 500C.

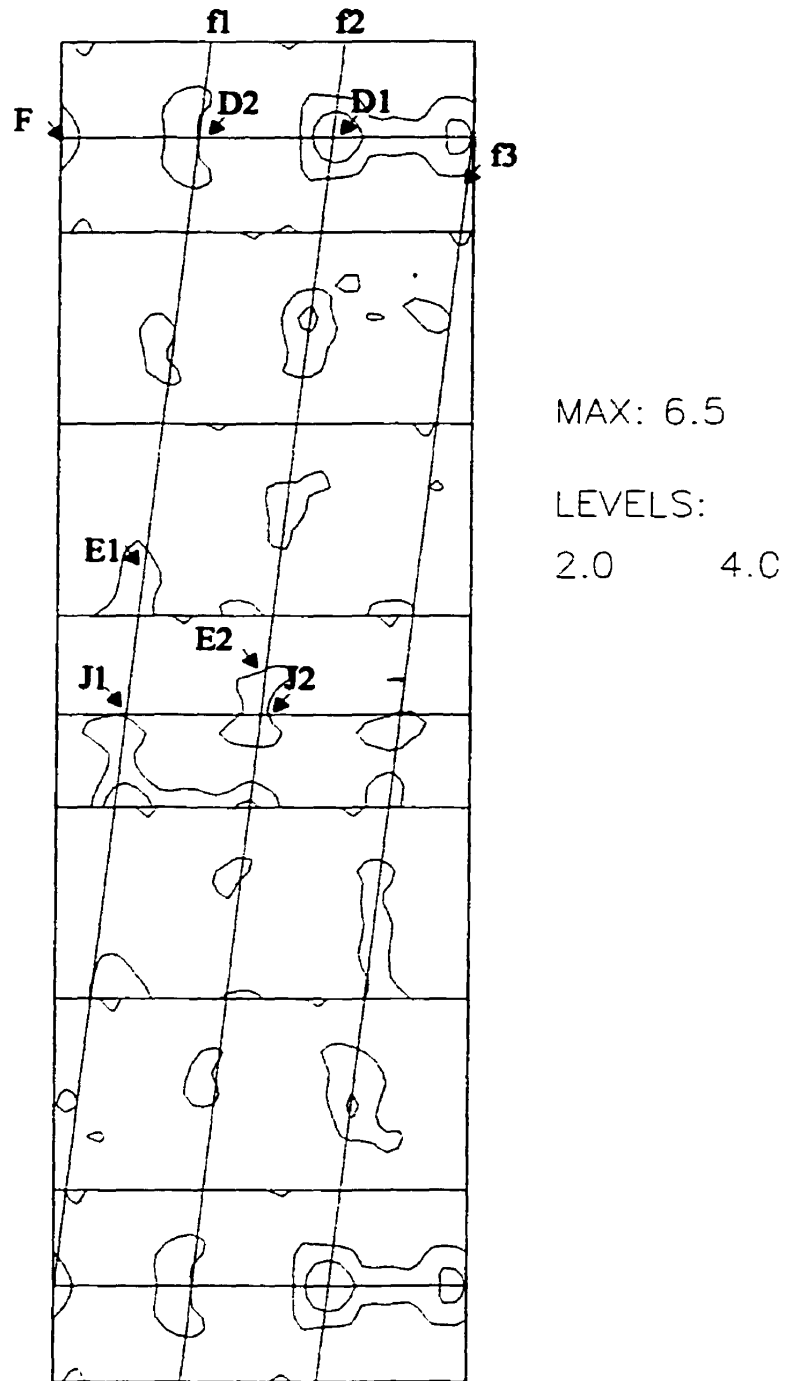


Figure 4.13 Ti IF deformed at 600 C.

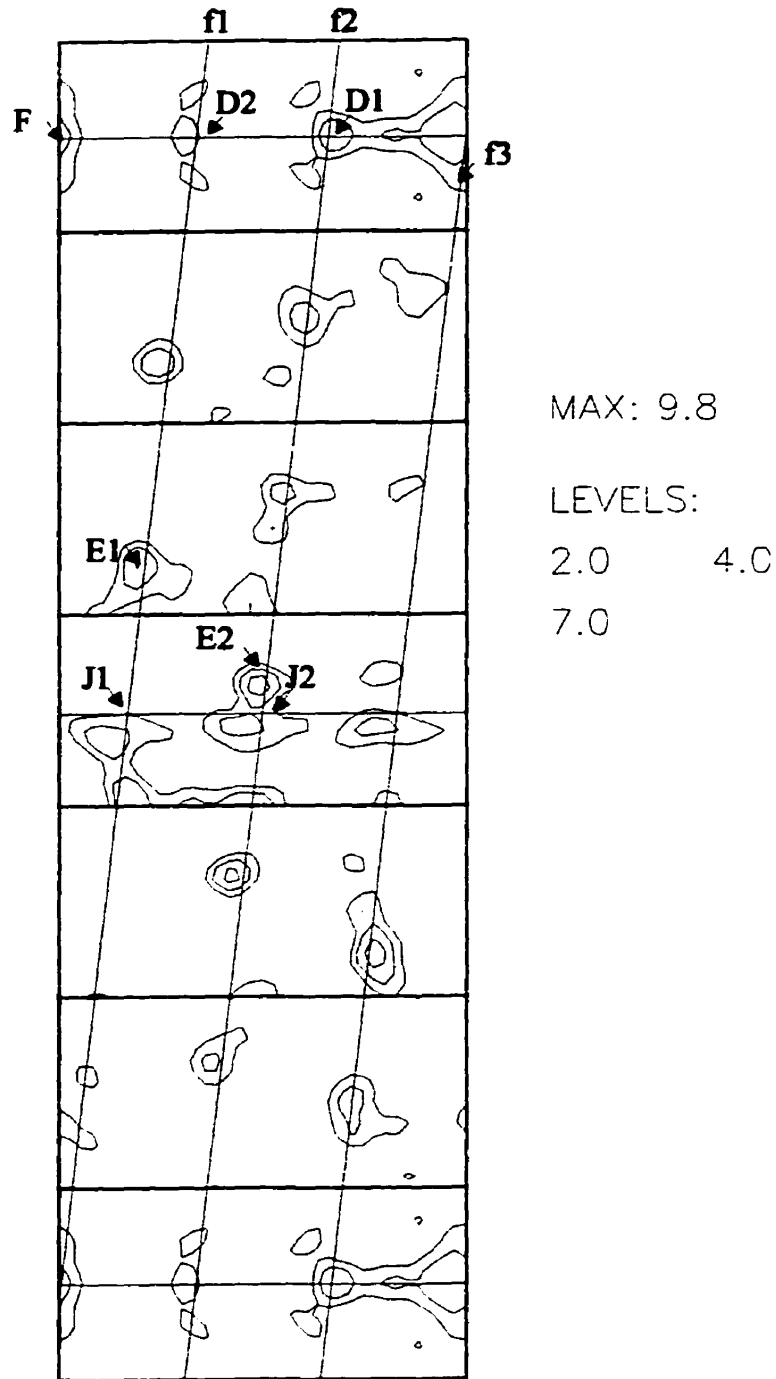


Figure 4.14 Ti IF 409 deformed at 700 C.

The textures of the titanium stabilized specimens deformed at 800°C and above show a markedly different form, Figs. 4.15-4.22. The intensities of the more highly deformed samples are several times greater than those of the room temperature texture. At the lower strain levels in the 800-1000°C specimen, textures there is little or no evidence of the occurrence of dynamic recrystallization. The J and F components in these textures remain important with respect to the other components. In addition, the maximum intensities remain relatively low. In the samples strained to higher levels at these temperatures, a new texture is seen. The maximum intensities are much higher than in the previous textures and the weights of the components have shifted dramatically. This higher temperature texture is interpreted here to be a dynamic recrystallization texture. In these samples, the D2 $(\bar{1}\bar{1}2)[111]$ component becomes by far the most important. The F and J components become quite insignificant in comparison to the D1 component as well, while the E1/E2 component remains constant in intensity.

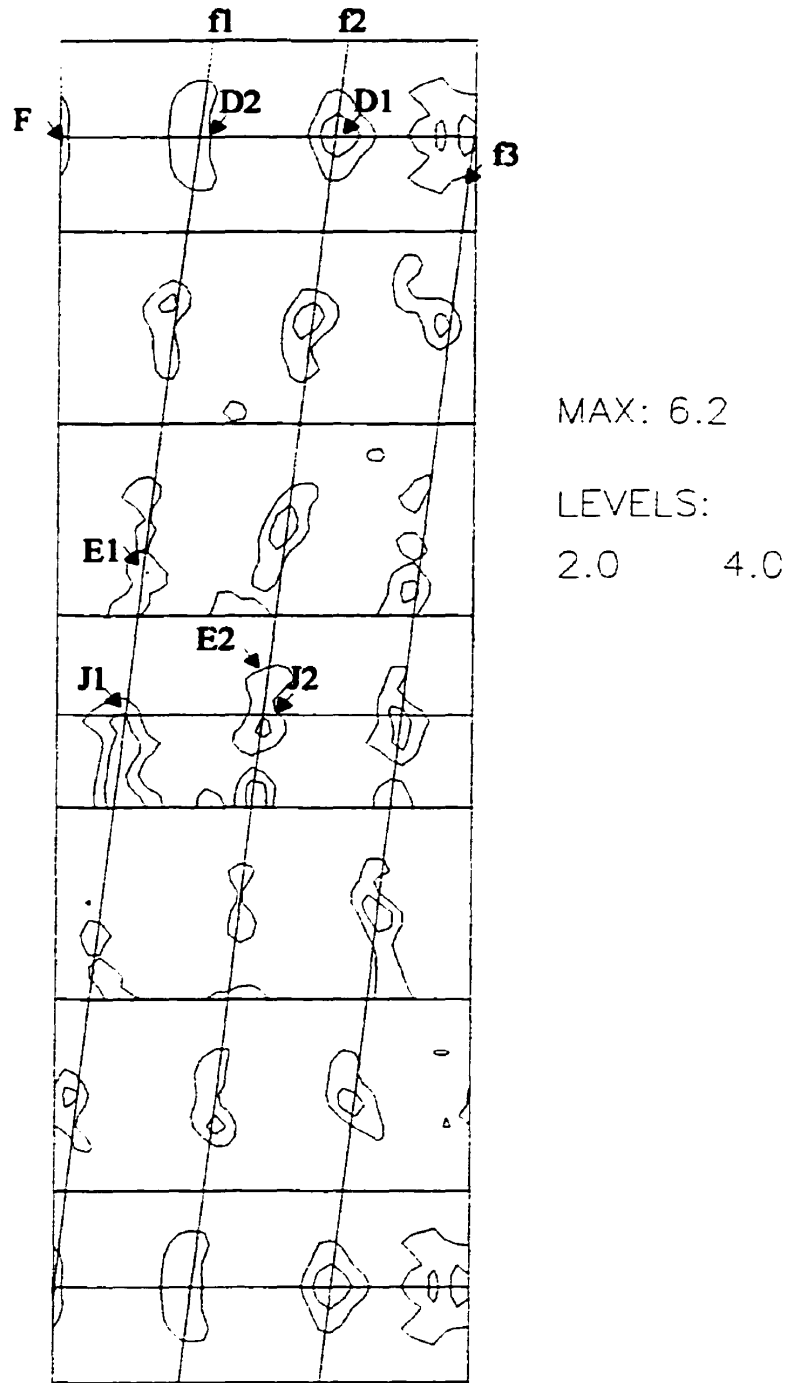


Figure 4.15 Ti IF 409 deformed at 800 C to low strain level.

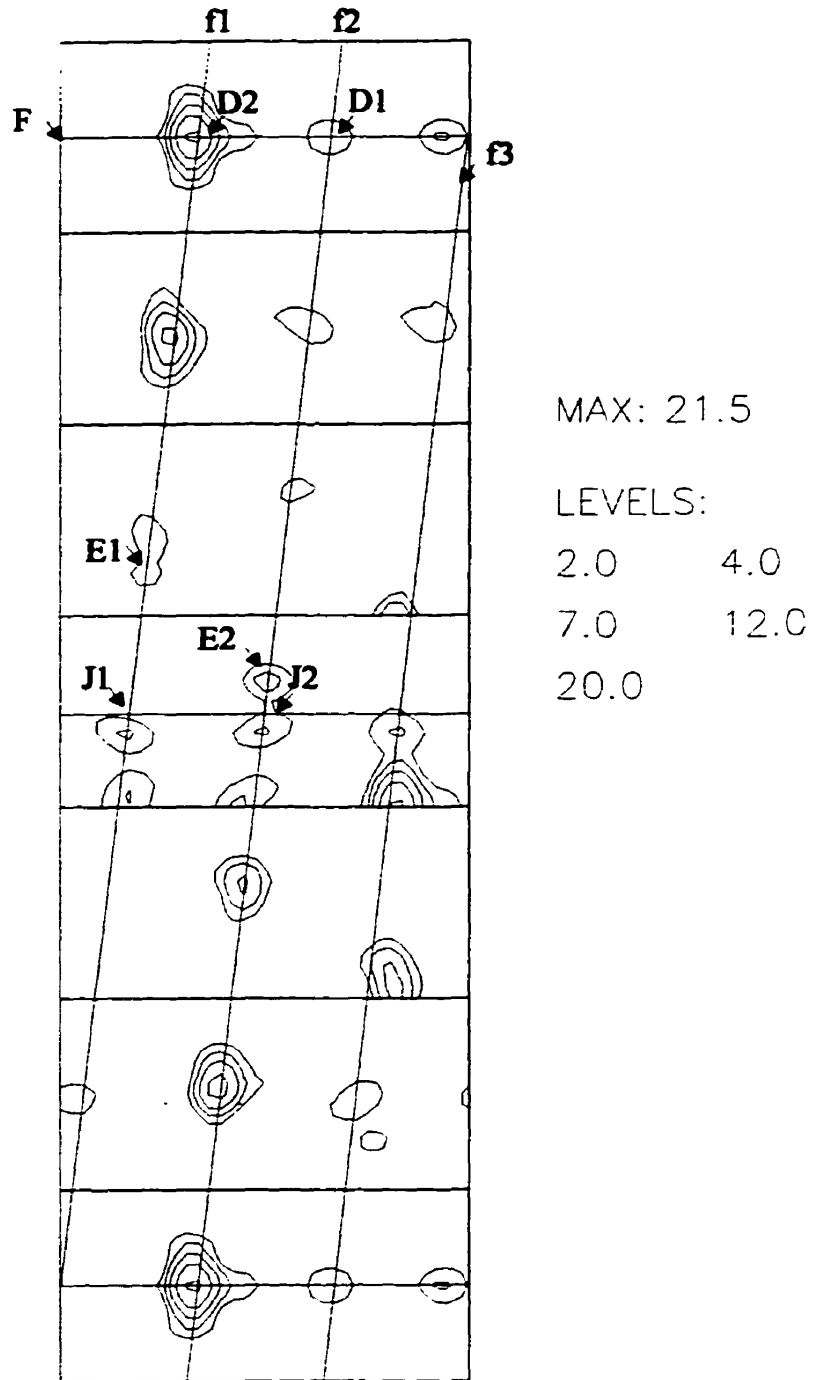


Figure 4.16 Ti IF 409 deformed at 800 C to high strain level.

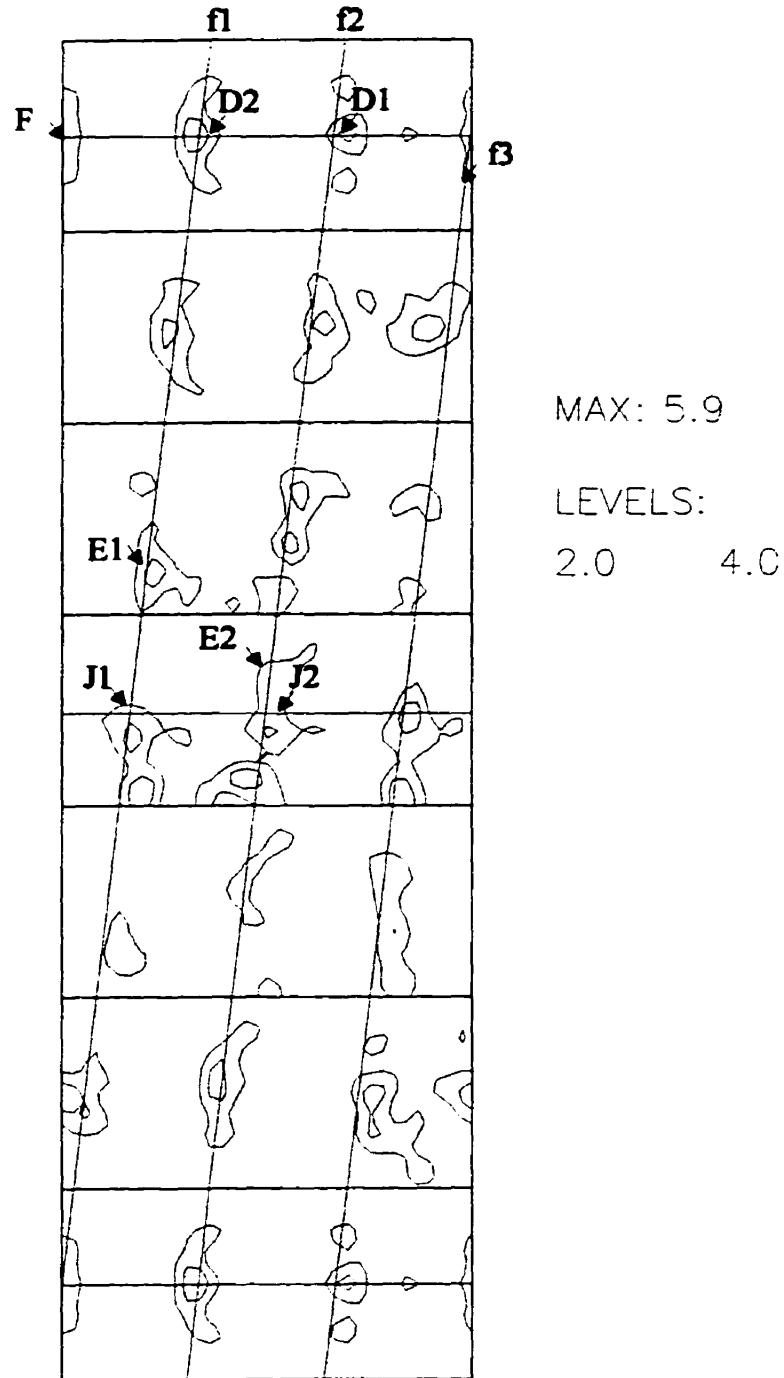


Figure 4.17 Ti IF 409 deformed at 900 C to low strain level.

Chapter IV Experimental Results

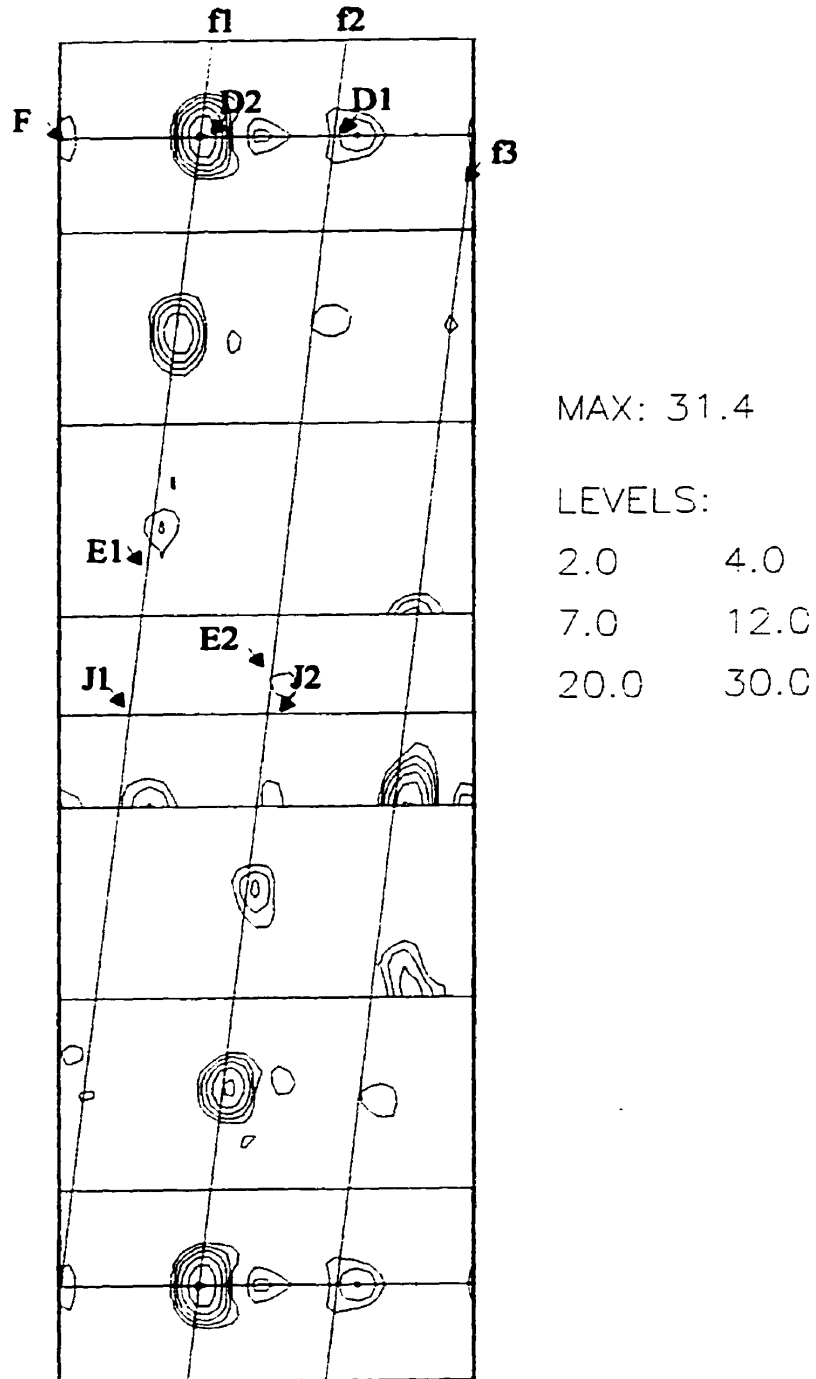


Figure 4.18 Ti IF 409 deformed at 900 C to high strain level.

Chapter IV Experimental Results

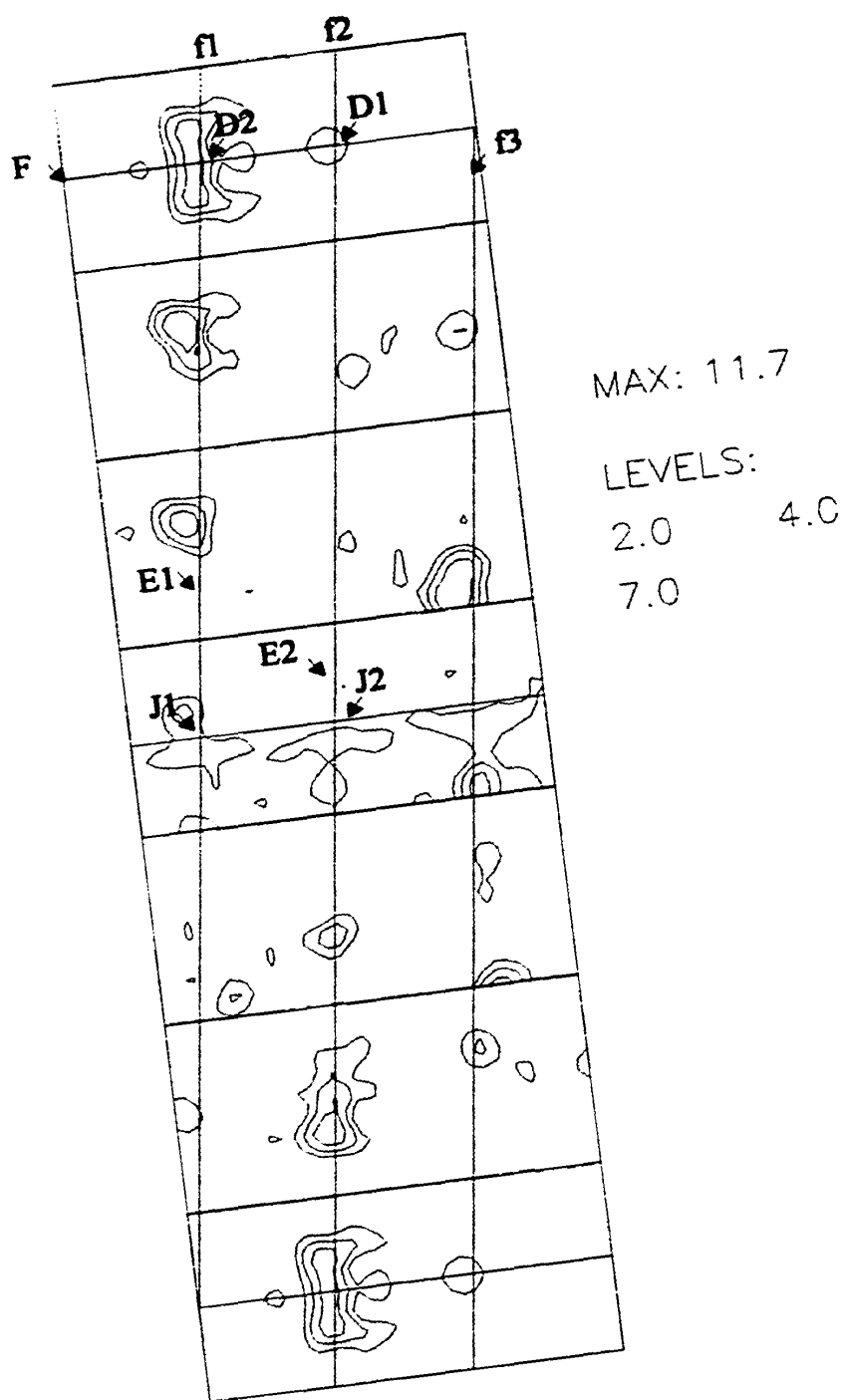


Figure 4.19 Ti IF 409 deformed at 1000 C to low strain level.

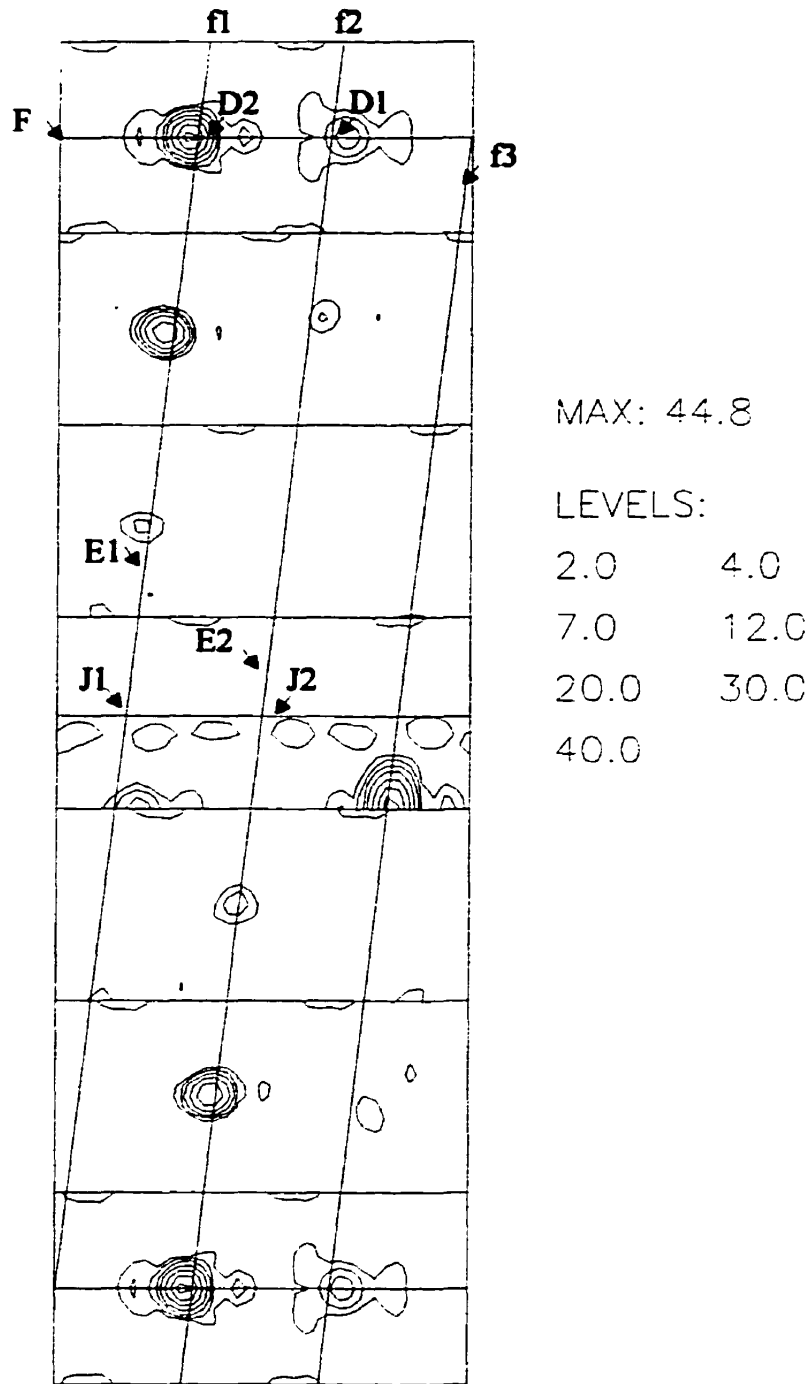


Figure 4.20 Ti IF 409 deformed at 1000 C to high strain level.

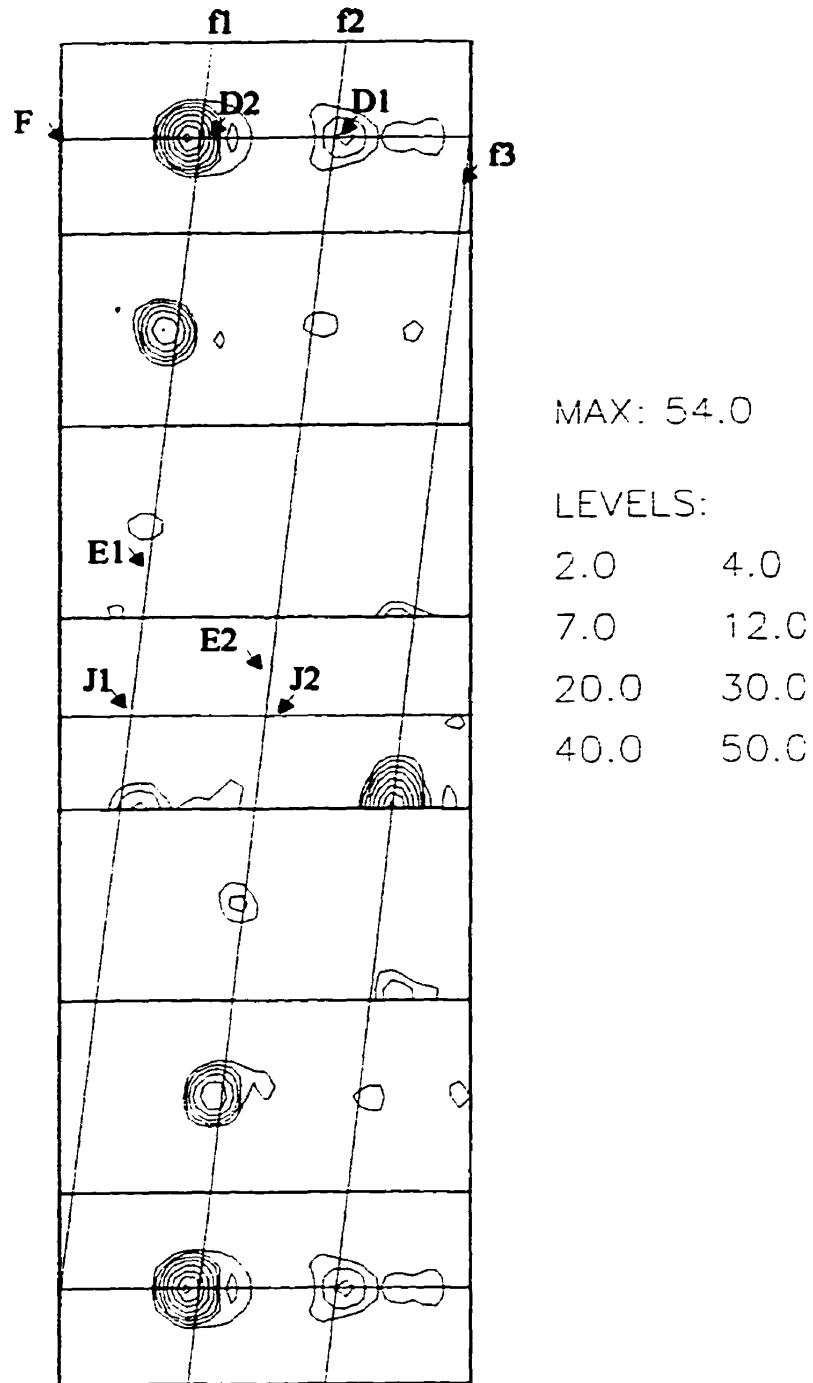


Figure 4.21 Ti IF 409 deformed at 1100 C to low strain level.

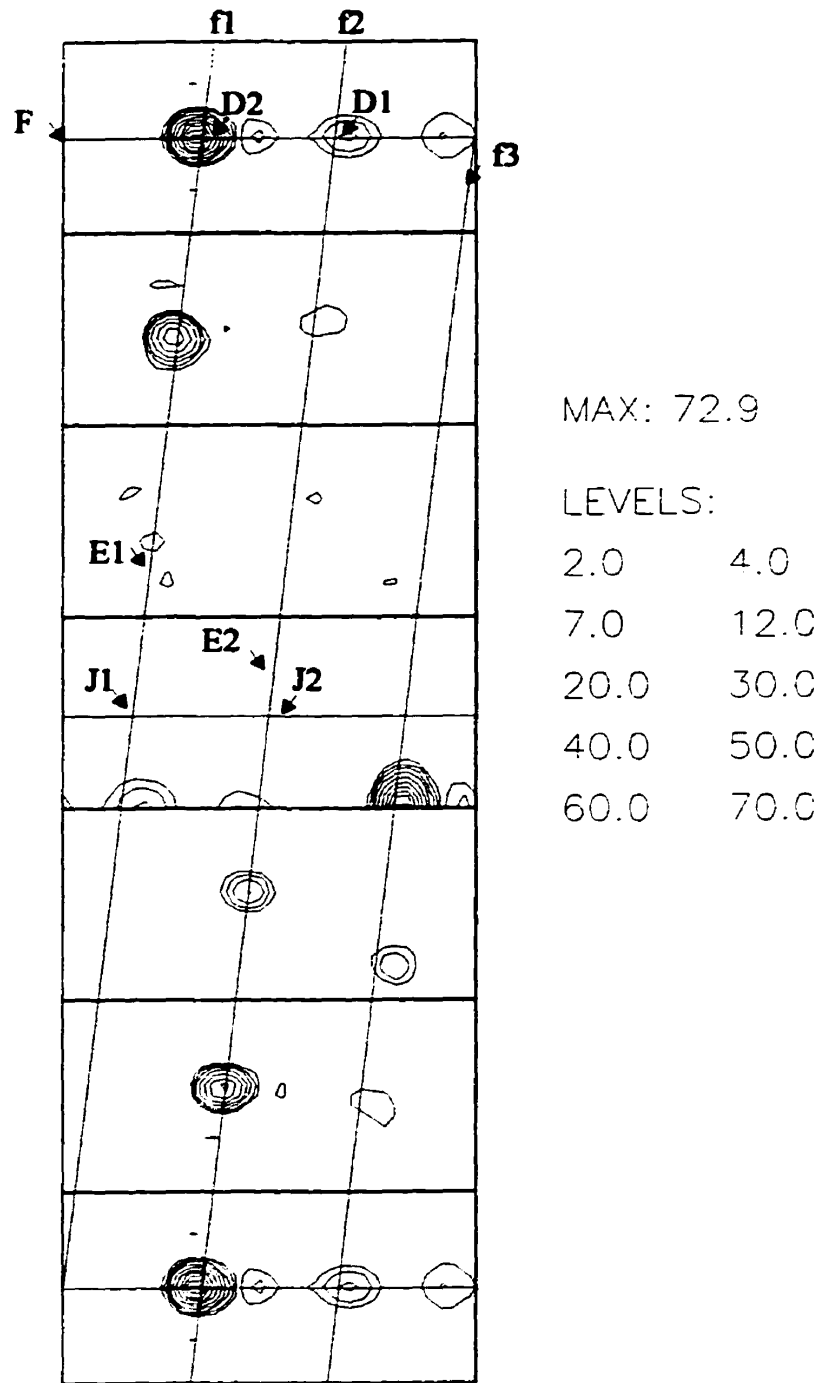


Figure 4.22 Ti IF 409 deformed at 1100 C to high strain level.

The titanium-niobium textures follow the same general pattern. In the textures of the specimens deformed at 700 and 800°C, the F and J components are quite important as with the room temperature sample, Figs. 4.23-4.24. The intensities remain low for both textures. As expected, the D1/D2 component increases while the J and F decrease as the temperature increases. However, the beginning of the transition can be noted in the 800°C texture.

The textures of the specimens deformed at 900°C and above show the occurrence of dynamic recrystallization, Figs. 4.25-4.28. As with the titanium stabilized steel, the D2 texture increases to become the primary component of the texture. Also, the J and F room temperature dislocation glide components decrease to the point of insignificance with respect to the D1/D2 components. Finally, the intensities of the textures tend to increase significantly as the temperature of deformation increases.

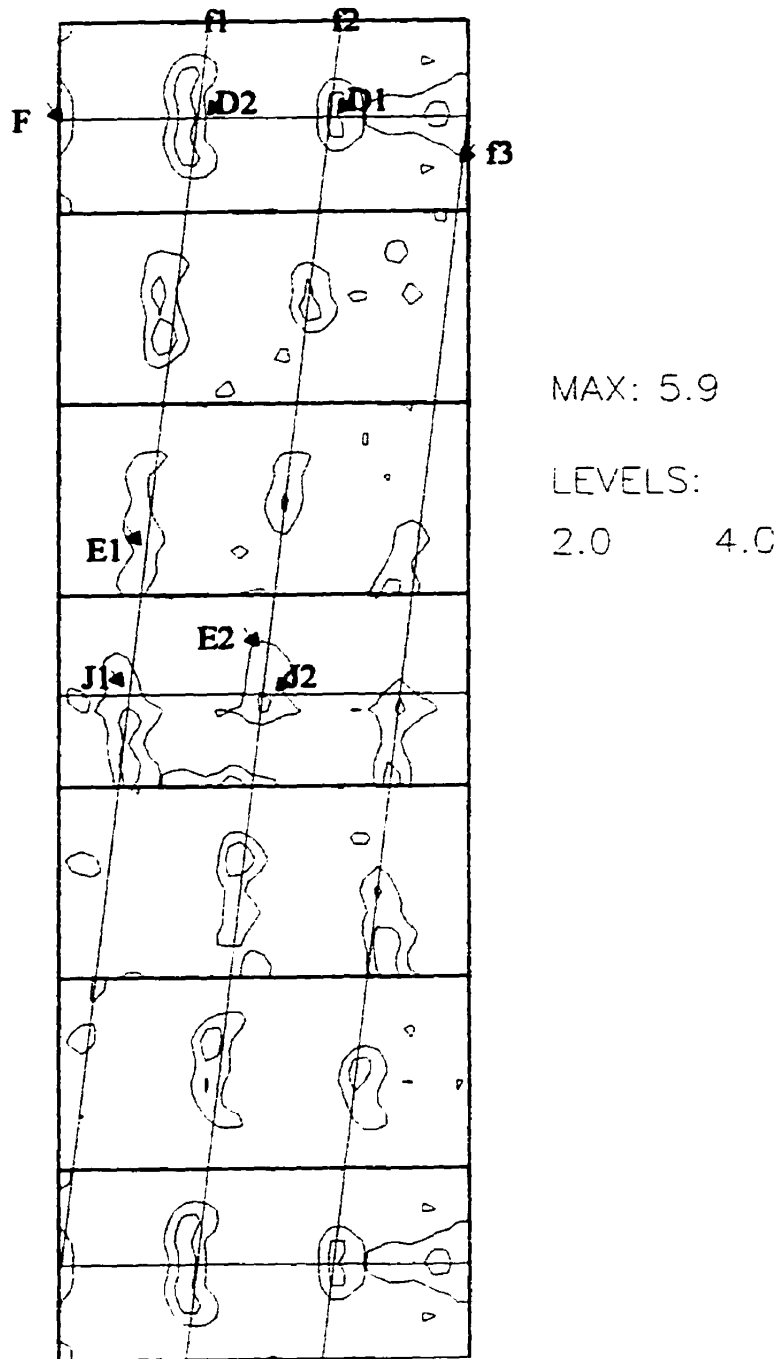


Figure 4.23 TiNb IF 409 deformed at 700 C.

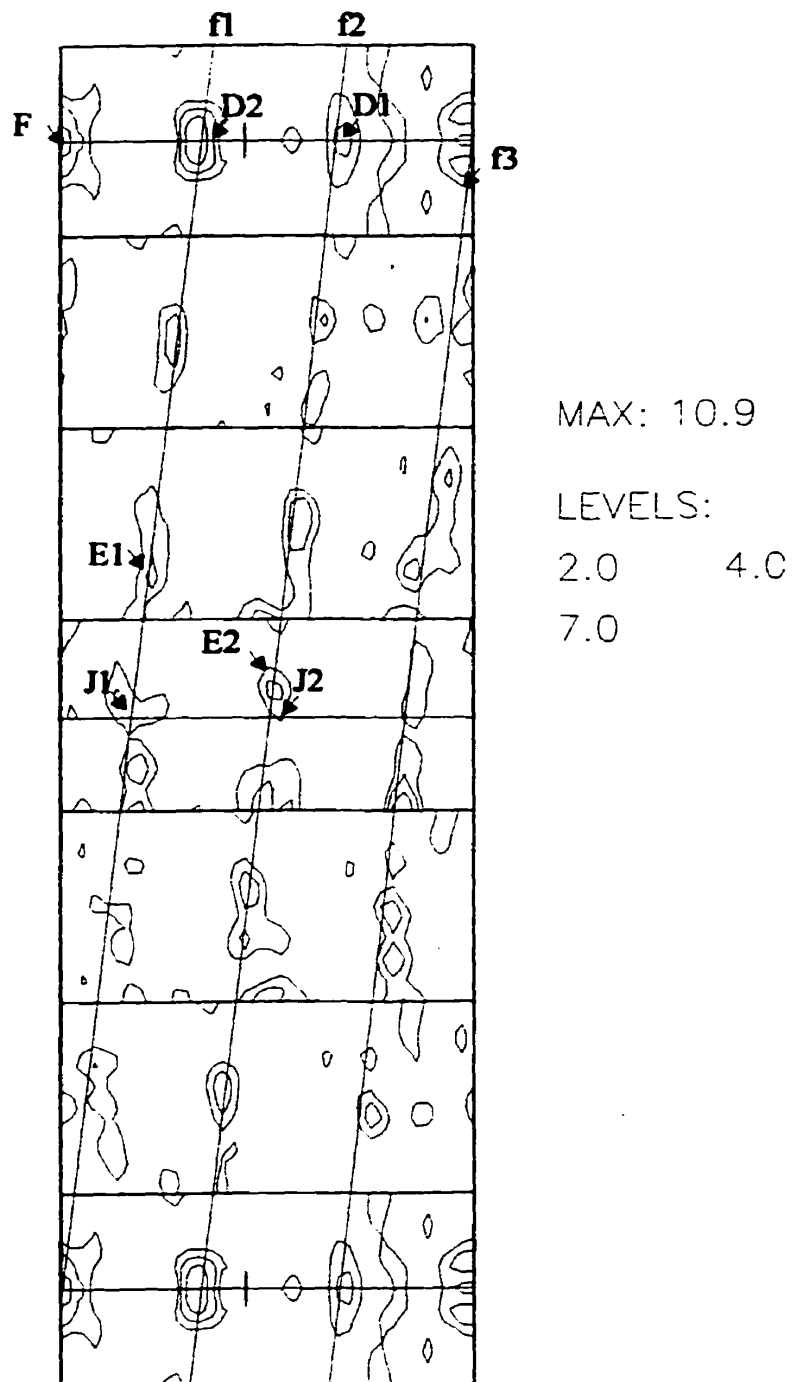


Figure 4.24 TiNb IF 409 deformed at 800 C.

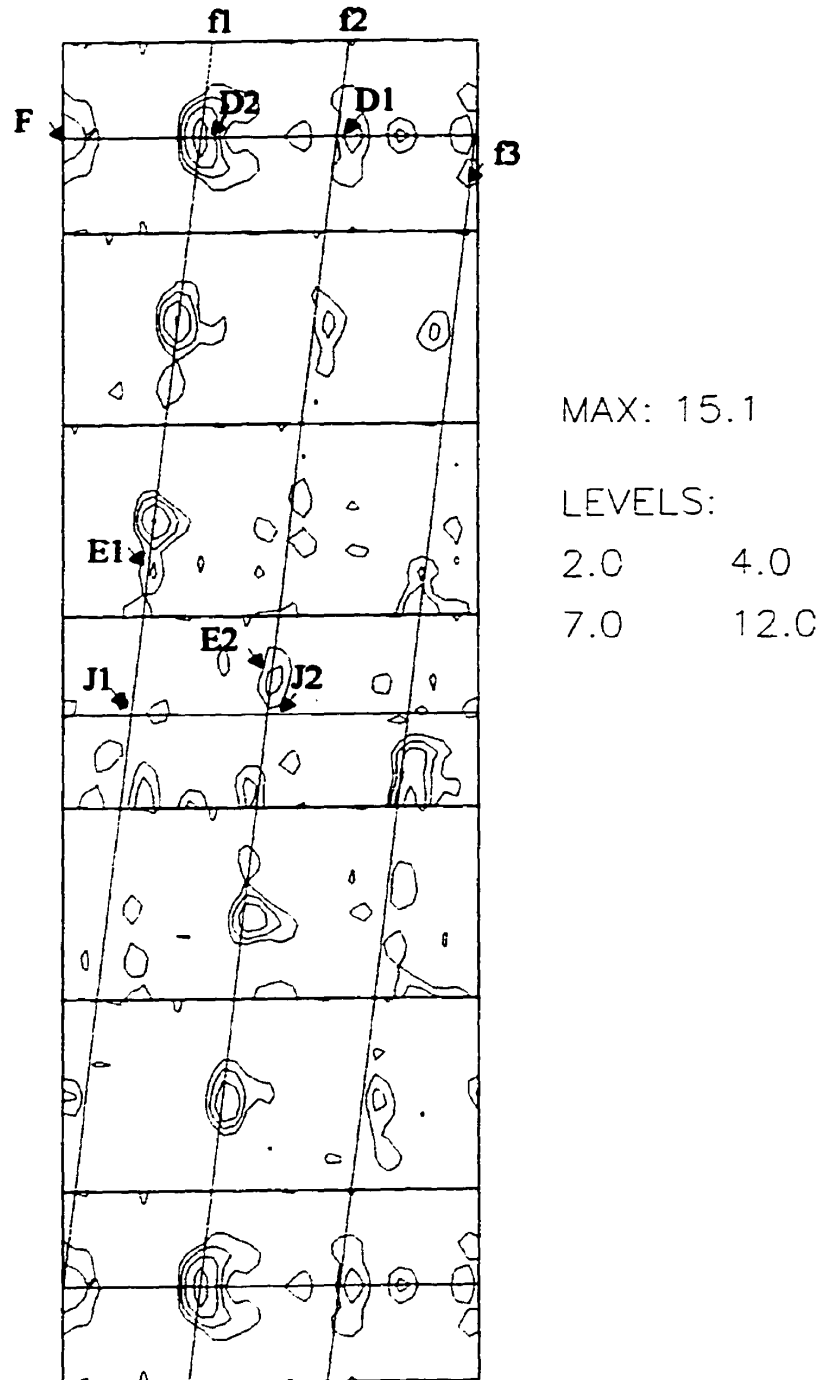


Figure 4.25 TiNb IF 409 deformed at 900 C.

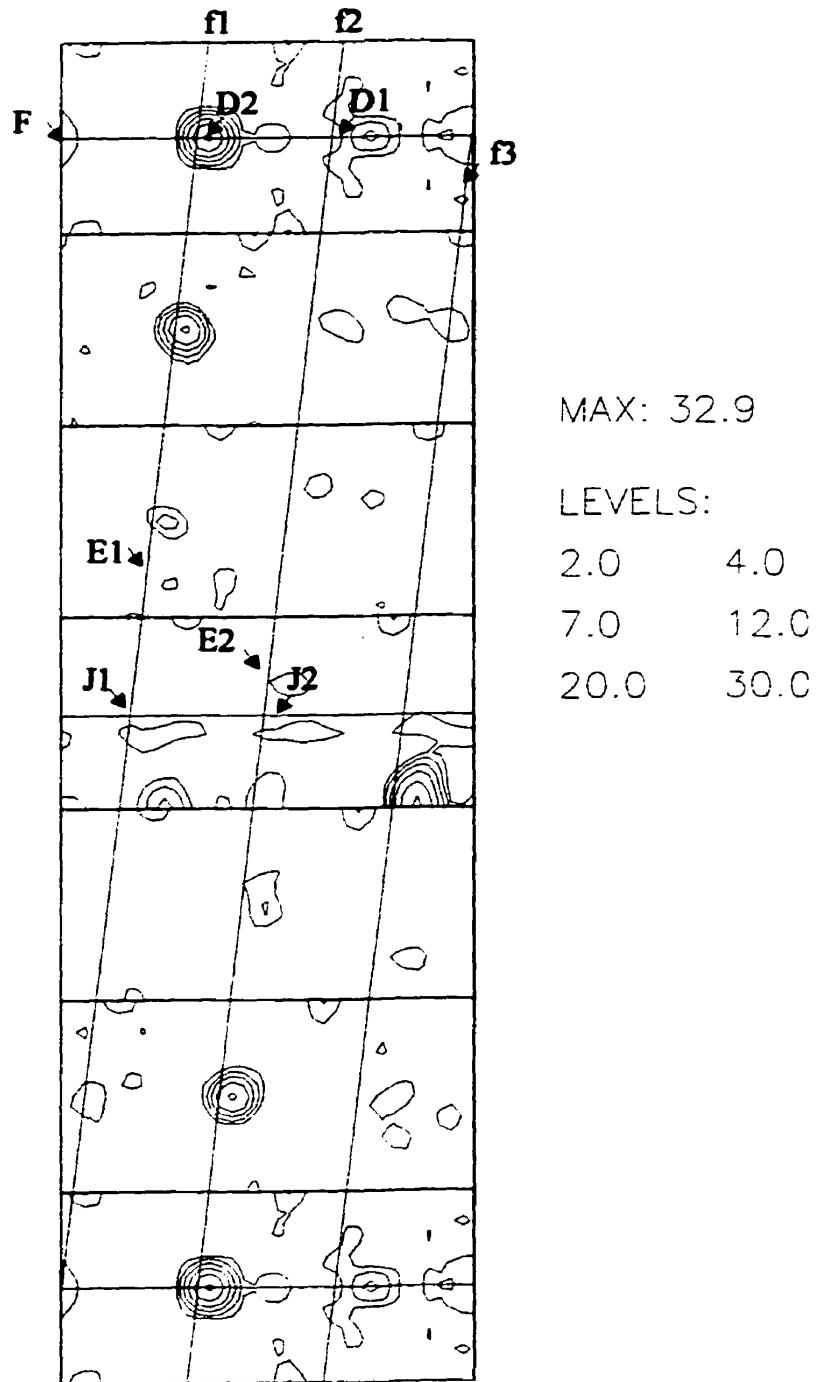


Figure 4.26 TiNb IF 409 deformed at 1000 C.

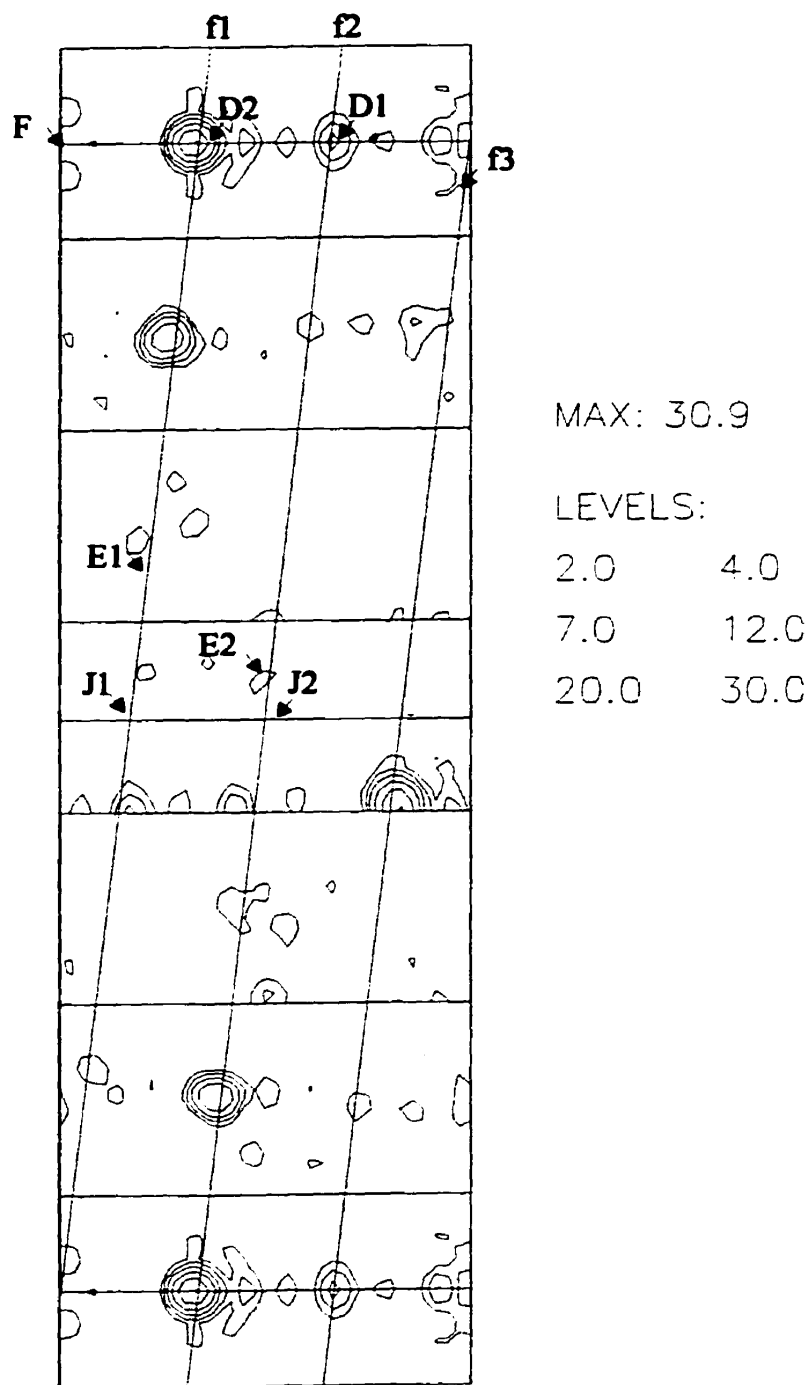


Figure 4.27 TiNb IF 409 deformed at 1100 C.

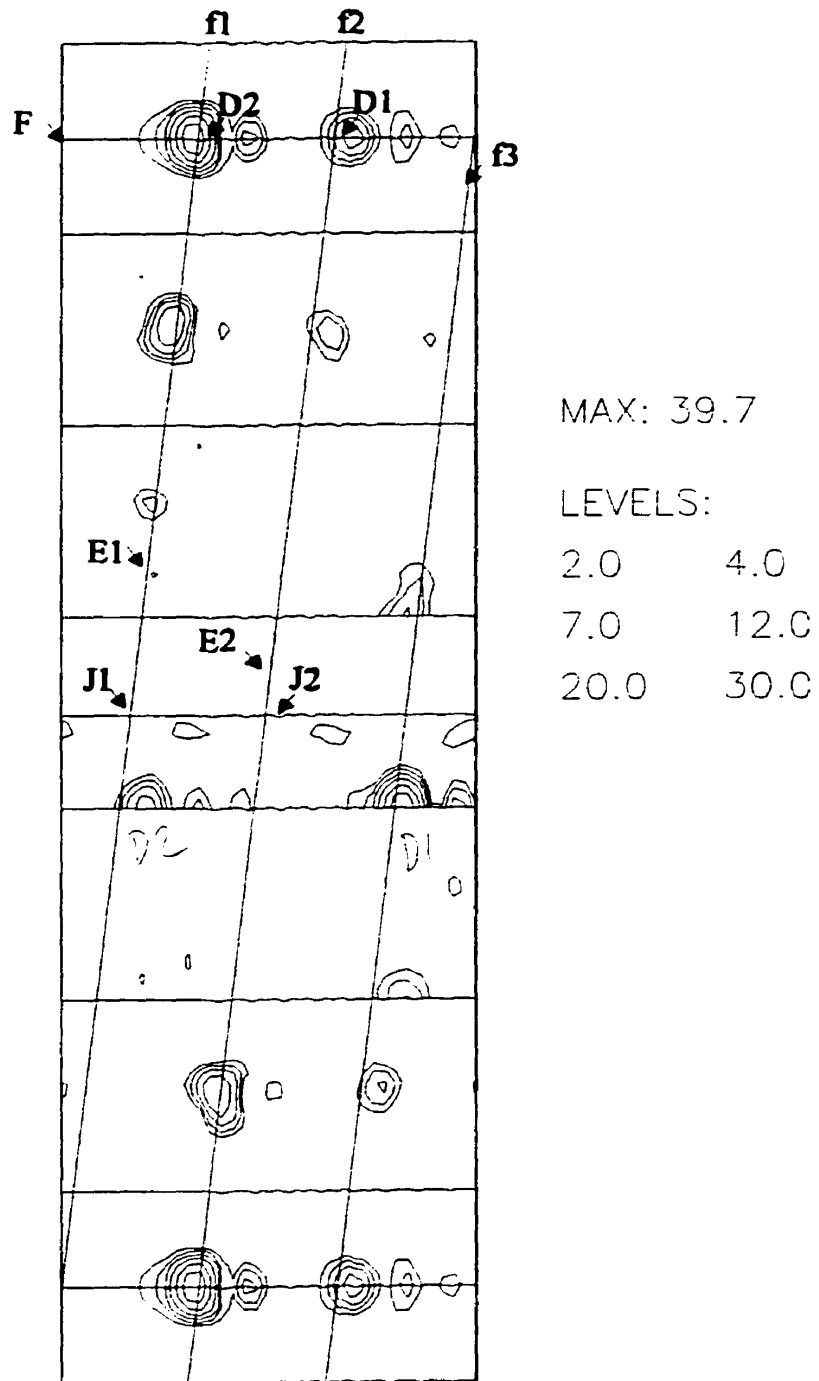


Figure 4.28 TiNb IF 409 deformed at 1200 C.

Chapter V

Discussion

5.1 General

The purpose of this work was to determine whether dynamic recrystallization could occur in ferritic IF stainless steel. Typically, this could be concluded from an examination of the flow curves of the deformed specimens. However, the flow curves of hot deformed BCC materials are not cyclic, and thus are not clearly indicative of dynamic recrystallization. Therefore, x-ray diffraction and texture measurement were used to analyze the softening behaviors of the two stainless steel grades. In addition, microstructural analysis was employed to supplement the textural work. The behavior of the steels at room temperature is important to note as none of the dynamic softening mechanisms is occurring. The flow curve, microstructural, and texture behaviors at room temperature display only deformation (i.e. glide) behavior. When the steels are deformed at high temperatures, the change in behavior obviously indicates the occurrence of one or more additional softening mechanisms. By analyzing the differences in behavior and comparing the changes to pre-existing models, the type of softening can be determined.

5.2 Room Temperature Behavior

The flow curves of both steels deformed at room temperature (Fig.4.3) follow the pattern of those in the literature. The titanium stabilized steel yielded at around 425 MPa and reached a peak stress of over 700 MPa. The titanium-niobium stabilized steel, on the other hand, yielded around 540 MPa and had a tensile strength of over 800 MPa. The curves displayed a very simple behavior. An interesting item is the small amount of work hardening that is characteristic of ferritic metals. The microstructures also provide insight into the behaviors of these steels. The starting microstructure of both steels consisted of a relatively equiaxed structure with a fairly large grain size (Figs.4.6a and 4.7a). After deformation, both display a highly elongated structure characteristic of cold work (Figs.4.6b and 4.7b).

5.3 Elevated Temperature Mechanical Behavior

Typically, the first approach to detecting the occurrence of dynamic recrystallization is by examination of the flow curves. If the flow curve is periodic, as displayed by most FCC materials that can be taken as indicative of dynamic recrystallization. If the maximum stress is followed by substantial flow softening, and then by a steady state region at a lower stress level as occurs at lower temperatures or higher strain rates in FCC metals, dynamic recrystallization is again believed to occur. In the present case, slight peaks were reached, but these were only slightly higher than the steady state region (Figs.4.4-4.5). In the absence of substantial flow softening, the flow curves did not provide clear evidence of dynamic recrystallization according to the criteria normally employed for FCC metals. However, as already pointed out above, there is not much work hardening in BCC metals, by comparison with FCC metals. Thus, the

former cannot be expected to display the same proportions of flow softening as the latter during the approach to the steady state. This is why the same criteria with regard to flow curve shape cannot be applied to the two classes of metals.

Nevertheless, there is a noticeable shift in flow curve shape from room temperature to elevated temperature. The room and lower elevated temperature curves show no tendency to decrease in flow stress once the peak is reached. By contrast, the highest temperature curves display a steady decrease in stress beyond the peak. Although this behavior could result from a testing artifact, the view is taken here that the shape change indicates that something is happening at high temperatures that is not happening at the lower temperatures. This interpretation is supported below in the discussion of the microstructural and texture observations

5.4 Microstructural Analysis at Elevated Temperatures

Another method commonly used to determine if dynamic recrystallization is occurring is microstructural analysis. Dynamic recrystallization involves the nucleation and growth of new, strain-free grains in the deformed matrix. These new grains are by definition smaller than the current grain size. Also, as a material is deformed, the grains rotate and elongate to facilitate the dimensional changes. These two effects allow for the recognition of dynamic recrystallization under certain conditions. In this case, both steels behave in a similar manner, Figs.4.6-4.7c&d. The titanium stabilized steel deformed at 600°C displays a highly elongated grain shape, resembling that of the room temperature specimen. For the titanium-niobium stabilized steel, the behavior at 700°C also resembles the behavior of the steel at room temperature.

By contrast, when deformed at the highest temperatures, both steels showed a quite different microstructure. The titanium stabilized steel had a relatively equiaxed structure with a finer grain size. The same thing is noticed in the titanium-niobium stabilized steel. These microstructures indicate that some form of new microstructural process is playing a role. When combined with the texture results discussed below, the two sets of observations provide a good indication that a type of dynamic recrystallization is occurring in these steel grades.

5.5 Torsion Textures at Elevated Temperatures

As mentioned above, two types of behavior were detected in the present investigation: the 'room temperature' family of results and the 'dynamic recrystallization' family. The 'room temperature' family was also displayed at elevated temperatures up to the dynamic recrystallization temperature. The 'dynamic recrystallization' family was found over the temperature range within which dynamic recrystallization was observed. Over the entire experimental range, the texture components increase or decrease in intensity. Since the texture observed at room temperature is obviously produced by dislocation glide followed by crystal rotation, if the textures at higher temperatures resemble the room temperature texture, it is apparent that the high temperature texture is likely to have been produced by the same mechanism and not by dynamic recrystallization. On the other hand, if the texture at some elevated temperature differs from that of the room temperature specimen, it can be suspected that some other mechanism is operating. This new mechanism can be detected by modeling the texture results; evidence can also be gathered from supporting experimental techniques, such as mechanical testing, microstructural characterization, and electron microscopy. One important step in determining the occurrence and extent of dynamic recrystallization is to

follow the changes in intensity of the critical texture components defined above as the temperature and strain levels are varied.

In the titanium stabilized steel, the component intensities evolve as the temperature is increased, Fig.5.1. In the room temperature texture, the J and F components, produced by glide, are the strongest. As the temperature of deformation increases through 400°C to 500°C, the J and F components remain important with respect to the other orientations. The other components: D1, D2, and E1/E2, all remain nearly constant at a relatively low intensity. At 600°C, the components begin to shift in importance. The D1 becomes the most intense orientation. In addition, the F and J components decrease in importance relative to the others. As the temperature increases to 700°C, the D1, D2, and E1/E2 components increase intensity with regards to the 'room temperature' components J and F. This temperature represents the highest point at which the room temperature deformation texture dominates, although some dynamic recrystallization has begun to take place to a small extent.

At 800°C, the texture is markedly different. The D2 component intensity increases from 3.0 to 20.1. Both the D1 and the E1/E2 remain important and the J and F components are now much less important. This texture is dominated by the mechanism responsible for dynamic recrystallization for the first time. In the range from 900 to 1100°C, the dynamic recrystallization texture becomes still more pronounced. The D2 component generally increases in intensity until it completely dominates all the others. The D1 component also remains significant, although it is much weaker than the D2. The remaining components become negligible.

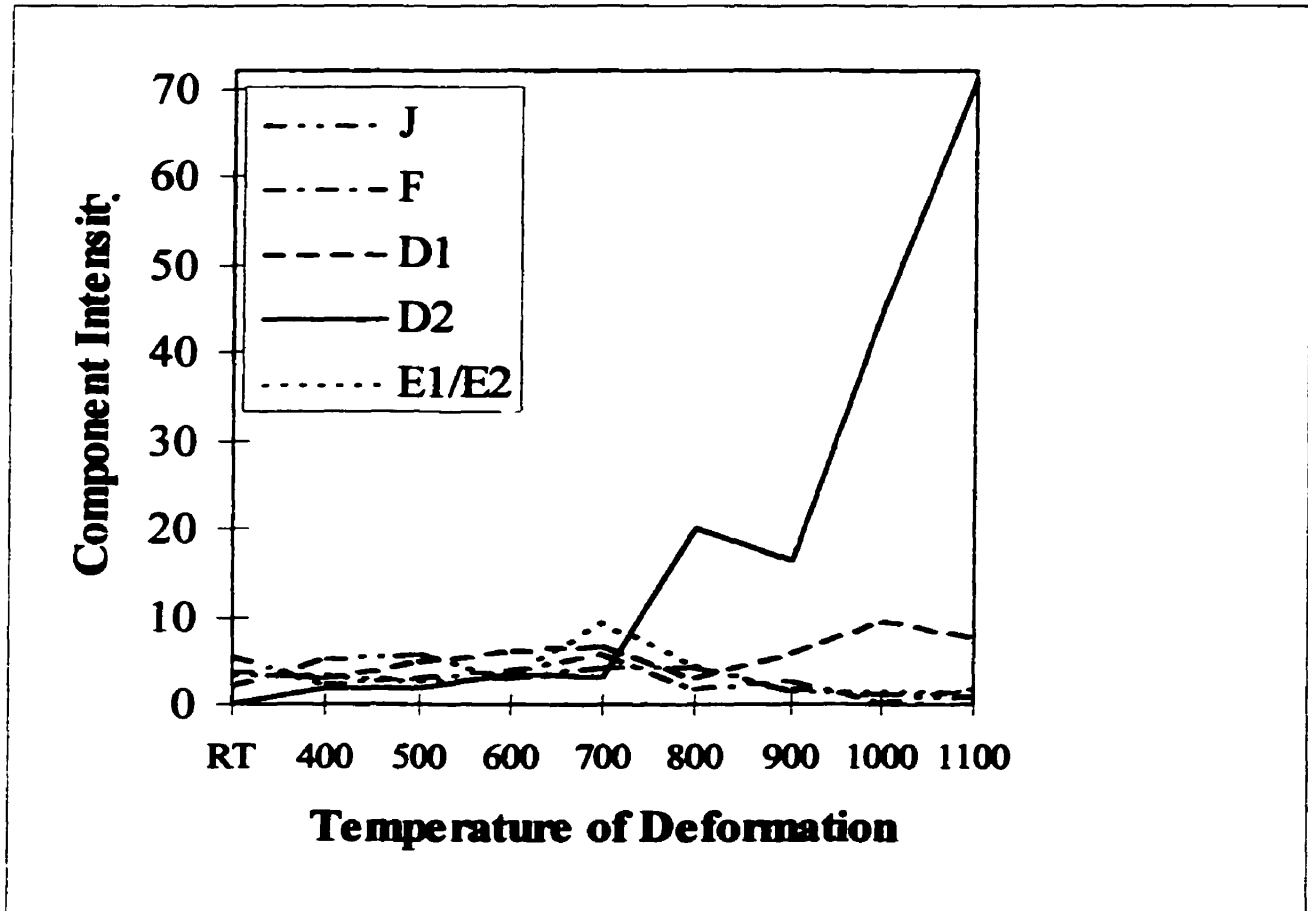


Figure 5.1 Ti Stabilized IF 409: effect of temperature on critical component intensity.

The behavior of the titanium-niobium stabilized steel is much the same as that of the titanium stabilized steel, Fig 5.2. The J and F glide components decrease in importance as the temperature increases. E1/E2 increases to 900°C, at which point it begins to decrease to an insignificant level. The D1 level generally increases and remains at a relatively high intensity, even at 1200°C. Most importantly, the D2 component increases slowly to around 1000°C, after which it increases at a rapid rate. As with the titanium stabilized steel, 700°C is the highest temperature at which the pure room temperature texture is displayed. However, the new, dynamic

recrystallization texture is not clearly apparent until 1000°C, although some recrystallization is certainly occurring at slightly lower temperatures. One interesting point is that, even at the higher temperatures, dynamic recrystallization is not occurring to the same extent in the titanium-niobium stabilized steel as in the titanium stabilized steel. The rate of increase in intensity of the D2 component with temperature, Fig. 5.2, is also lower than in the case of the titanium stabilized steel, Fig. 5.1.

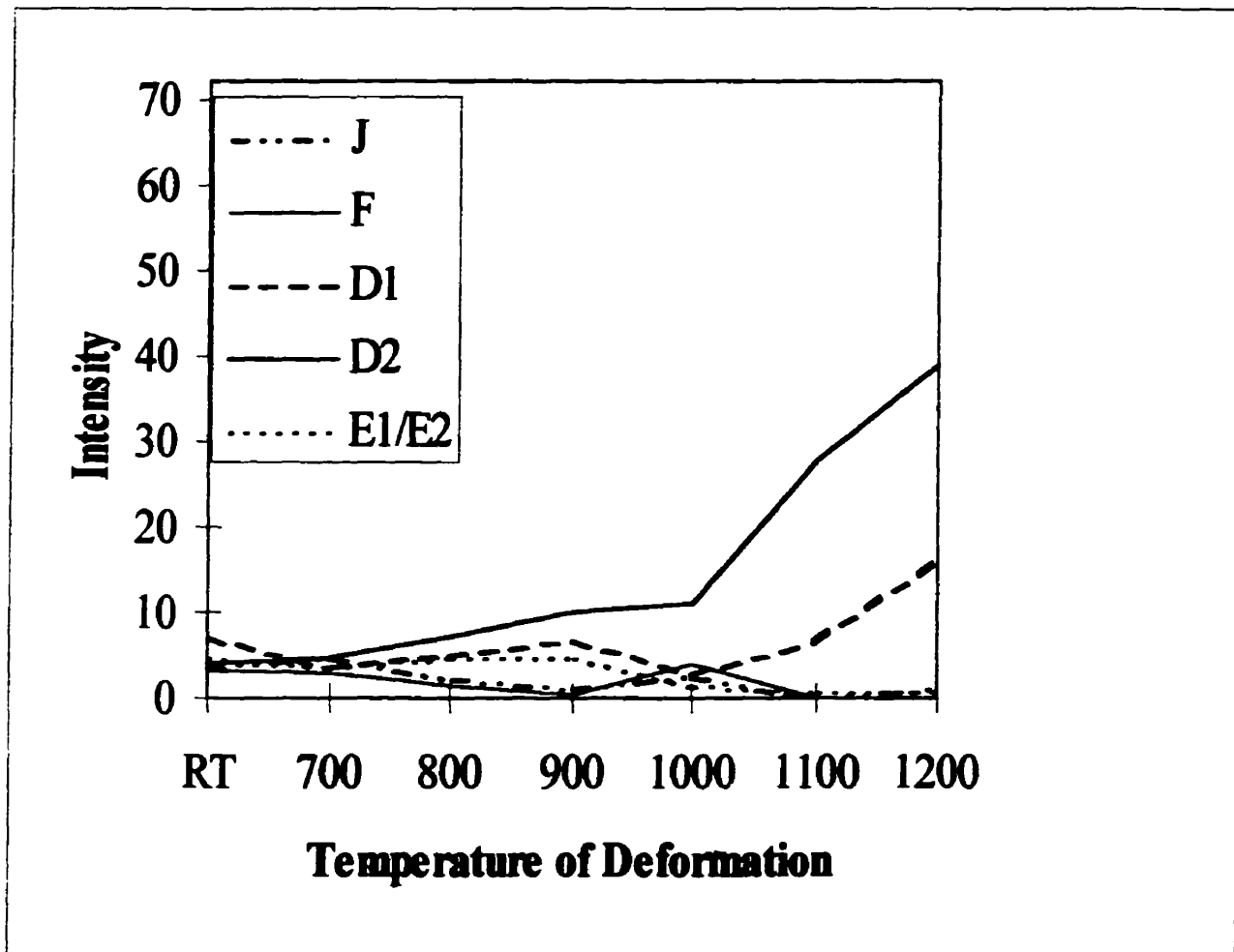


Figure 5.2 TiNb Stabilized IF 409: effect of temperature on critical component intensity.

5.6 Importance of the D2 Component

The progress of dynamic recrystallization in the present materials was measured primarily in terms of the intensity of the D2 component in this work. Baczynski [39] developed a model to predict dynamic recrystallization textures in ferritic metals. In this model and in his experimental results, Baczynski found the D2 component to be predominant when dynamic recrystallization occurred. He was able to show using glide simulations that recovery was not responsible for the increasing intensity of the D2 component. Instead, he concluded that the D2 component intensity was enhanced by grain boundary migration, specifically by the occurrence of dynamic recrystallization. Baczynski states that the increase in the strength of this component results from the low stored energy nucleation of low Taylor factor nuclei. These nuclei grow uniformly, not selectively, which provides the huge increases in the strength of the D2 component at higher temperatures.

Other work supports the Baczynski model of occurrence regarding the oriented nucleation during continuous dynamic recrystallization in ferritic metals. Dillamore *et al.* [66] found the same type of behavior during the conventional static recrystallization of α -iron and two commercial low-carbon steels. In addition, recent work by Kestens and Jonas [67] regarding static recrystallization in electrical steels showed that oriented nucleation played a critical role in forming the annealing texture, while selective growth played only a minor role.

In this work, the D2 components display a behavior qualitatively similar to that described by Baczynski [39], Fig.5.3. All of the results share a similar pattern, although the D2 intensities at a given temperature

depend on the composition of the steel. The D2 component remains at a relatively low and constant level until dynamic recrystallization occurs. When dynamic recrystallization is initiated, the D2 intensity increases drastically. In the interstitial-free ferritic steels examined in Baczynski's work, both titanium and titanium-niobium stabilized, the temperature at which dynamic recrystallization begins to operate is considerably lower, a difference that will be discussed below. The interstitial-free ferritic stainless steels that are the subject of the current work have D2 intensities which, once dynamic recrystallization occurs, do not increase to the same degree. In general, however, the similarities are obvious when the behaviors of the two sets of steels are compared.

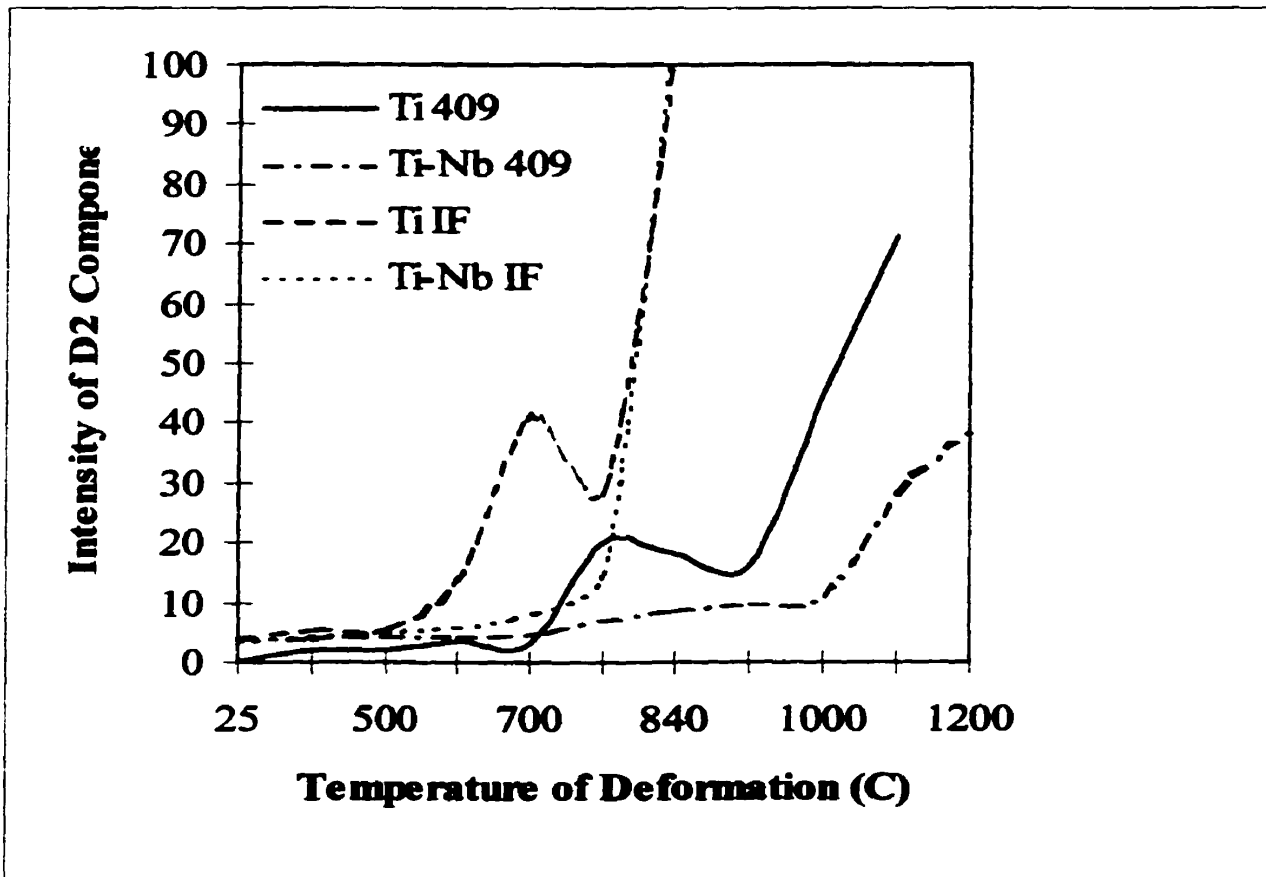


Figure 5.3 Effect of temperature on D2 components of various IF steel grades.

5.7 Continuous Dynamic Recrystallization

Continuous dynamic recrystallization is associated with the flow curves and microstructures found in the current work and is typical of ferritic metals. The discontinuous dynamic recrystallization observed in austenitic steels is quite different. Discontinuous recrystallization is typically found in low and medium stacking fault energy FCC metals, see Section 2.5.7 above. The present flow curves displayed a slight maximum followed by a steady state region. No oscillations or multiple peaks, associated with discontinuous dynamic recrystallization, were observed under any conditions. The microstructural results also support this conclusion. Discontinuous recrystallization typically nucleates along grain boundaries, producing a characteristic by 'necklace' structure, see Section 2.5.2.2.1. This structure consists of a series of small, nuclei surrounding a larger, older, and deformed grain. The recrystallized structures in this work, Section 4.3, are characterized by a very tight distribution of grain sizes rather than by the large/small distribution expected if 'necklacing' had occurred.

These results are also supported by the literature. The work by Dillamore *et al.* [66] mentioned above concluded with the observation that 'the most likely nucleation process is that of subgrain growth, no grain boundary nucleation events having been observed'. In addition, Montheillet [68] noticed similar trends in his experiments on the high temperature, high strain deformation of aluminum. Montheillet used additional experimental techniques such as EBSP, SEM, and TEM to prove that equiaxed subgrains were formed at low strains ($\epsilon < 1$ for torsion) and that the misorientations within particular grains remained small (less than 15°). This behavior led to the appearance of 'clouds' of orientation points located around the orientations of the original grains on a pole figure.

These clouds disappeared at large strains, because the low angle grain boundaries associated with the subgrains were transformed into high angle grain boundaries during continuous dynamic recrystallization in aluminum [68].

The mechanisms involved in the transition from the low strain to the high strain behavior are still unknown, but two models have been proposed. The first model, suggested by Perdrix *et al.* [69], proposed that mobile dislocations are being absorbed continuously by the subgrain boundaries at low strains, leading to higher and higher misorientations. The second model, proposed by McQueen *et al.* [70], is known as 'geometric dynamic recrystallization', and is particularly applicable to very large strains.

5.8 Static Recrystallization Kinetics

The present work concerns the occurrence of dynamic recrystallization in BCC metals. Obviously, it is important to prevent the start of static or post-dynamic recrystallization. The softening curves, Figs. 4.1-4.2, show that post-dynamic recrystallization is initiated at around 50 and 110 seconds for the titanium and titanium-niobium stabilized steels, respectively. As mentioned above, the quench times are considerably shorter, from 2 to 4 seconds.

5.9 Effect of Chemical Composition

In both the present work and that of Baczynski [39], the effect of the type of stabilization was evident. The dual stabilized steel, containing titanium and niobium, underwent post-dynamic and dynamic recrystallization at higher temperatures than the titanium stabilized steel. The superior recrystallization retarding effect of niobium is seen in many

different systems as well [71]. In the present work, the softening curves and texture results clearly show the effect of the presence of niobium. Titanium only retards recrystallization as a precipitate. As the titanium precipitates are coarser than the niobium precipitates, the pinning effects of titanium are reduced. Niobium can retard recrystallization whether in solution or as a precipitate.

In addition to preventing the onset of dynamic recrystallization at lower temperatures, the textures formed by dynamic recrystallization in the dual stabilized steel are not as intense as those formed in the titanium stabilized steel, Fig. 5.3. The maximum intensity in the titanium stabilized steel deformed at 1100°C was 72.9. At 1200°C, the maximum intensity in the dual stabilized steel was 39.7. At a higher temperature, the niobium still produced a weaker texture. The same behavior occurred in the steels studied by Baczynski. The recrystallization temperature was higher in the dual stabilized steel. Also, the texture produced in the dual stabilized steel was not as strong as that formed in the titanium stabilized steel. Obviously, these results are related to the presence of niobium as a stabilizing element. Large amounts of work have been carried out on the effects of niobium as a stabilizing element [72]. It is apparent that the presence of niobium retarded the initiation of dynamic recrystallization at the lower temperatures and slowed the progress of dynamic recrystallization at the higher temperatures.

Chapter VI

Conclusions

In the current work, the torsion textures produced by deformation and by continuous dynamic recrystallization were generated and analyzed in two interstitial-free 409 stainless steels. These steels were deformed over the temperatures range, 20 to 1200°C. Supplementary tests were run to ensure that dynamic softening was the only softening occurring, i.e. that static softening did not play an important role. The two types of textures generated were compared and analyzed. The main conclusions of this work are as follows:

1. The flow curves of the two steels were similar at room temperature. The work hardening rate at a given strain decreases with temperature, eventually leading to saturation and a steady state region. At higher temperatures, a slight maximum is noticed; in addition, the flow stress decreases slightly with increasing strain.
2. The room temperature textures of the two steels consist of the three characteristic fibers: f1, f2, f3. The texture consists of the important individual components F $\{110\}\langle 001\rangle$, J $\{110\}\langle 211\rangle$, E $\{001\}\langle 111\rangle$, and D $\{112\}\langle 111\rangle$.

3. The texture in the titanium stabilized steel at 800°C differs markedly from those observed at lower temperatures. The D2 component is very intense, with the D1 and E1/E2 components also important. This is attributable to continuous dynamic recrystallization. The J and F glide components are also still present. The same transition is noticed in the dual stabilized grade at 1000°C, although the rate of recrystallization is somewhat slower.

4. The dynamic recrystallization textures of the steels consist of the D2 $(\bar{1}\bar{1}2)[111]$, D1 $(11\bar{2})[111]$, and E2 $(0\bar{1}1)[111]$ individual components. The D2 component becomes increasingly important as the strain is increased, which leads to the relative weakening of the D1 and the disappearance of the E2 component at very large strains.

5. The dynamic recrystallization textures observed in the two steels can be accounted for by the operation of the low stored energy nucleation mechanism. The growth of the nuclei was uniform, as opposed to selective. This supports the theory of oriented nucleation in the present case.

6. Continuous (in situ) dynamic recrystallization was occurring in the present steels. A single slight maximum was observed in the flow curves when dynamic recrystallization was taking place. This observation was supported by the microstructural work, which showed that a narrow distribution of grain sizes was present as opposed to the more varied size distribution expected with discontinuous dynamic recrystallization.

7. Niobium retards the development of dynamic recrystallization textures. Less softening and less dynamic recrystallization occur under given

Chapter VI Conclusions

conditions in the titanium-niobium stabilized steel than in the titanium grade. In addition, the strength level at room temperature is higher in the niobium steel.

References

1. R.A. Lula, Stainless Steel, ASM, Metals Park (1986).
2. R. Castro, "Historical Background to Stainless Steels", Stainless Steels, ed. P. Lacombe, B. Barroux, and G. Beranger, Les Editions de Physique, Les Ulis, 1 (1993).
3. L. Guillet, Rev. Metal., 1 155 (1904), 2 350 (1905), 3 372 (1906).
4. A. Portevin, Iron and Steel Institute, Carnegie Scholarship Memoirs, 1, 230 (1909).
5. W. Giesen, Iron and Steel Institute, Carnegie Scholarship Memoirs, 1, 1 (1909).
6. P. Monnartz, Metallurgica, 8, 161-176 (1971), (1932).
7. H. Hansen, Constitution of Binary Alloys, McGraw-Hill, 52 (1958).
8. E. Baerlecken *et al.*, Stahl und Eisen, 81, 768 (1961).
9. F.B. Pickering, "Physical Metallurgy of Stainless Steel Developments", International Metals Reviews, 10 (1976).
10. E.C. Bain and R.H. Aborn, Metals Handbook, ASM, 1194 (1948).
11. D. Chandra and L.H. Schartz, Metall. Trans., 2 (1971).
12. H.J. McQueen and J.J. Jonas, "Recovery and Recrystallization During High Temperature Deformation", Treatise on Materials Science and Technology, Vol. 6: Plastic Deformation of Materials, ed. R.J. Arsenault, Academic Press, NY, 393 (1975).
13. L.G. Byrne, Recovery, Recrystallization, and Grain Growth, Macmillan, NY (1965).
14. H. Hu, "Recovery, Recrystallization, and Grain Growth", Metallurgical Treatises, TMS-AIME, 385 (1981).
15. R.W. Cahn, "Recovery and Recrystallization", Physical Metallurgy, ed. R.W. Cahn and P. Hansen, 1595 (1983).
16. P. Cotterill and P.R. Mould, Recrystallization and Grain Growth in Metals, Surrey Univ. Press, London (1976).
17. R.W.K. Honeycombe, The Plastic Deformation of Metals, 2nd Ed., Edward Arnold, 293 (1984).

18. J.D. Verhoeven, Fundamentals of Physical Metallurgy, John Wiley and Sons, NY (1975).
19. F.R.N. Nabarro, Acta Metallurgica, **37**, 1521 (1984).
20. V.M. Sample *et al.* "Dynamic Softening of Copper During Deformation at High Temperatures and Strain Rates", Acta Metallurgica, **35**, 367-379 (1987).
21. H.M. McQueen and J.J. Jonas, Journal of Applied Metal Working, **3**, 233 (1984).
22. M.J. Luton and C.M. Sellars, Acta Metallurgica, **17**, 1033 (1969).
23. W. Roberts, "Deformation, Processing, and Structure", 1982 ASM Materials Science Seminar, ed. G. Krauss, ASM, Metals Park, 109 (1984).
24. C. Roucoules, Ph.D. Thesis, McGill University, Montreal (1992).
25. R. Sandstrom and R. Lagneborg, Acta Metallurgica, **23**, 387 (1975).
26. W. Roberts and B. Ahlblom, Acta Metallurgica, **26**, 801 (1978).
27. G.J. Richardson, *et al.*, Acta Metallurgica, **14**, 1221 (1966).
28. C. Ouchi and T. Okita, Trans. ISIJ, **22**, 543 (1982).
29. H.J. McQueen and S. Bergerson, Metal Science, **6**, 25 (1972).
30. G. Gottstein, L. Lang, and H.F. Yung, Mat. Sci. And Tech., **7**, 158 (1991).
31. C.M. Sellars, Proc. 7th Int. Symp. On "Metallurgy and Materials Science", eds. N. Hansen *et al.*, Risø National Laboratory, Roskilde, Denmark, 167 (1986).
32. L. Fritzemeier *et al.*, "Strength of Metals and Alloys", Proc. Conf., ICSMA5, eds. P. Haasen *et al.*, Pergamon Press, NY, **1**, 95 (1979).
33. A. Wantzen *et al.*, "Strength of Metals and Alloys", Proc. Conf., ICSMA5, eds. P. Haasen *et al.*, Pergamon Press, NY, **1**, 517 (1979).
34. T. Sakai and M. Dhashik, Materials Science Technology, **6**, 1251 (1990).
35. G. Glover and C.M. Sellars, Metall. Trans., **4**, 765 (1973).
36. A. Najafi-Zadeh, J.J. Jonas, and S. Yue, Metall. Trans, **23A**, 2607 (1992).
37. H.J. McQueen *et al.*, 34th MWSP Conference Proc., ISS, Warrendale, 186 (1992).
38. N.D. Ryan, H.J. McQueen, *et al.*, 32nd COM, CIMM, 165 (1993).
39. J. Baczynski, Ph.D. Thesis, McGill University, Montreal (1996).
40. H.E. Hargreaves *et al.*, The Relation between the Structure and Mechanical Properties of Metals, NPC Symposium, 209 (1963).

41. R. W. Cahn, "Recrystallization of Single Crystals after Plastic Bending", Journal of Institute of Metals, **76**, 121 (1949).
42. R. W. Cahn, "Internal Strain and Recrystallization", Progress in Metals Physics, **2**, 151 (1950).
43. R. W. Cahn, "Recovery and Recrystallization", Physical Metallurgy, ed. R. W. Cahn, North-Holland, Amsterdam, 925 (1965).
44. R. W. Cahn, "A New Theory of Recrystallization Nuclei", Proceedings of the Royal Society, **A63**, 323 (1950).
45. H. Hu, "Direct Observation on the Annealing of a Si-Fe Crystal in the Electron Microscope", Trans. AIME, **224**, 75 (1962).
46. D. W. Bainbridge *et al.*, "Recent Observations on the Motion of Small Angle Dislocation Boundaries", Acta Metallurgica, **2**, 322 (1954).
47. P. A. Beck and P. R. Sperry, "Effect of Recrystallization Texture on Grain Growth", Trans. AIME, **185**, 240 (1949).
48. S. S. Gorelik, Recrystallization in Metals and Alloys, MIR Publishers, Moscow (1978).
49. M. Avrami, "Kinetics of Phase Changes, I, General Theory", Journal of Chemical Physics, **7**, 1103 (1939).
50. C. M. Sellars, Czech. J. Phys. **B35**, 239 (1985).
51. R. A. Petkovic *et al.*, Can. Met. Quart., **14**, 137 (1975).
52. W. T. Lankford *et al.*, "New Criteria for Predicting the Press Performance of Deep Drawing Sheets", Trans. ASM, **42**, 1197 (1950).
53. ASTM, Correlation of Deep-Drawing Press Performance with Tensile Properties, ASTM Special Technical Publication 390, Philadelphia (1965).
54. D. J. Blickwede, "Sheet Steel--Micrometallurgy by the Millions", ASM. Trans. Quart., **61**, 651 (1968).
55. R. S. Burns *et al.*, "Orientation and Anisotropy in Low-Carbon Steel Sheets", Sheet Metal Industries, **35**, 261 (1958).
56. D. V. Wilson, "Plastic Anisotropy in Sheet Metals", Journal of the Institute of Metals, **94**, 84 (1966).

57. H. Hu, "Texture of Metals", Texture, **1**, 233 (1974).
58. H.J. Bunge, "Representation of Preferred Orientations", Preferred Orientation in Deformed Metals and Rocks: An Introduction to Modern Texture Analysis, Academic Press, Inc., 73 (1985).
59. S.L. Semiatin *et al.*, ASM Metals Handbook, 9th Edition, Metals Park, **8**, 154 (1985).
60. P.R. Cetlin *et al.*, Metal. Trans, **24A**, 1543 (1993).
61. G.R. Canova *et al.*, ASTM STP, **753**, 189 (1982).
62. W.G. McGregor Tegart, Elements of Mechanical Metallurgy, Chapter 3, Macmillan, New York, 64 (1966).
63. D.S. Fields and W.A. Backhofen, Proc. ASTM, **57**, 1259 (1957).
64. G.F. Vander Voort, Metallography: Principles and Practice, McGraw-Hill, NY (1984).
65. P. Van Houtte *et al.*, Proc. ICOTOM 6, ed. S. Nagashima, ISIJ Tokyo, 428 (1981).
66. I.L. Dillamore *et al.*, Metal. Sci. Journal, **1**, 49 (1967).
67. L. Kestens and J.J. Jonas, Metall. Trans., **27A**, 155 (1996).
68. F. Montheillet, Les traitements thermomécaniques, 24ème Colloque de Métallurgie de Saclay, INSTN, Paris, 57 (1981).
69. Ch. Perdix *et al.*, Mem. Sci. Rev. Metall., **78**, 309 (1981).
70. H.J. McQueen *et al.*, Phil. Mag., **A60**, 473 (1989).
71. L.J. Cuddy, Thermomechanical Processing of Microalloyed Austenite, TMS-AIME, Warrendale, 129 (1982).
72. A.J. DeArdo *et al.*, Niobium, ed. H. Stuart, TMS-AIME, Warrendale, 685 (1981).